SLAC–PUB–3580
CERN–TH.4125/85
March 1985
(T/E)

TOPONIUM PRODUCTION IN e^+e^- COLLISIONS*

S. GÜSKEN

Institute for Theoretical Physics, RWTH Aachen
D-5100 Aachen, West Germany

and

J. H. KÜHN

CERN, CH-1211 Geneva 23, Switzerland

and

P. M. ZERWAS

Stanford Linear Accelerator Center
Stanford University, Stanford, California, 94305

Submitted to *Nuclear Physics B*

* Work supported by the Department of Energy, contract DE-AC03-76SF00515, and the West German Science Foundation DFG.

ABSTRACT

We study the properties of toponium states and their production in e^+e^- collisions with special emphasis on the mass region accessible to SLC and LEP. A formalism for toponium $-Z$ mixing is developed that is applicable for arbitrary mass differences between Z and the toponium state. It is shown that simple lowest order perturbation theory is equivalent to the mixing formalism up to an accuracy better than one percent in the entire energy range we investigate. The results are illustrated by calculations performed in the framework of two QCD inspired potential models which predict about 10 narrow states in the mass range around the Z. The mixing effects on the properties of Z are small even in the case of degenerate Z and toponium masses. The effect of electroweak interferences on and around toponium are studied, and analytic forms for cross sections and asymmetries before and after energy smearing are presented. We show that high radial excitations of toponium states below threshold may be difficult to disentangle from the continuum states. A brief survey of the properties of heavy bottom type quarkonia concludes the paper.

1. INTRODUCTION

Recent experimental results from the proton-antiproton collider[1] indicate a top quark mass of about 40 GeV. This value places toponium into a mass range where electroweak effects dramatically influence its production and decay properties. Since toponium and Z could be very close in mass, the problem of toponium-Z mixing must thoroughly be investigated. Last but not least our renewed interest has been stimulated by the fact that details of toponium properties are of importance for the experiments planned in the e^+e^- colliders under construction.

We therefore present a discussion of toponium production in e^+e^- annihilation that is applicable to the case of near mass degeneracy as well as for a quarkonium system well below or above the Z. Its influence on cross sections and asymmetries, before and after smearing over the beam energy spread, will be calculated analytically and the peculiar aspects of the threshold region will be investigated. Our paper is organized as follows.

Section 2 is devoted to the static properties of toponium states and to toponium-Z mixing. The formulae relevant for S and P-wave decays are collected and the general framework of toponium-Z mixing is set up. This formalism is cast in such a form that it can be applied to arbitrary mass differences between toponium and Z. In this way we expand on earlier papers on toponium decay properties[2,3] and a previous investigation of the mixing problem.[4] Our results, as we will show, coincide to a high degree of accuracy with lowest order perturbation theory. This is to be expected for such small mixing angles as predicted from a reasonable set of wave functions and coupling constants for toponium states. It is illustrated by calculations based on two specific potential models. Energy levels of all narrow states, decay rates and branching ratios are presented over the full range accessible to quarkonium physics in the near future. For the lowest levels our results are in accord with those of Ref. [5].We parametrize the energy levels, Γ_{ee}, $(R'_P(0)/m^2)^2$ and electric dipole transitions as a function of

the quark mass by a few coefficients so that they can easily be used for other applications. This section will be concluded by analyzing the influence of the whole set of narrow toponium states on the mass and width of the Z itself.

Section 3 is specifically devoted to the production of toponia in e^+e^- annihilation. We first shall briefly discuss the "direct" decays and then concentrate on the fermion-antifermion cross section, polarization phenomena, forward-backward and azimuthal asymmetries.[6,7] These observables determine the electroweak charges of the top quark[6] ; those are a necessary ingredient to extract the strong forces between quarks from the production rate in e^+e^- collisions. Interference between the resonant and the continuum cross section is of utter importance in this case. The apparent cross section is strongly modified by smearing over the beam energy spread, and we shall therefore present *analytic* results for all these quantities before and after averaging over the beam profile.

The properties of high radial excitations and the transition from the resonance region below the open top threshold to the continuum region are treated in Section 4.

In Section 5 we briefly touch the changes to be made for the case of a fourth generation bottom type quark. Conclusions are presented in Section 6.

Earlier work related to the subject of weak interactions of toponia, and not yet mentioned above, is listed in Refs. [8-18]. Brief accounts of parts of our results on toponium-Z mixing effects and the behavior of the e^+e^- cross section near the threshold for open top production can be found in Refs. [19, 20].

2. STATIC PROPERTIES OF TOPONIUM AND TOPONIUM-Z MIXING

2.1 General framework

It has frequently been stated in the literature that production and decay of a sufficiently heavy toponium state will proceed through a complicated mixture of electromagnetic and weak amplitudes. In particular, if the mass of toponium happens to be in the range $m_Z \pm 10\ GeV$, neutral current effects will dominate its properties. One way to describe this situation is through lowest order electroweak perturbation theory[6] —another one through toponium-Z mixing.[4] In this section we shall demonstrate that the two schemes lead to equivalent results—up to corrections which amount to less than 1% even in extreme cases. This holds true for all mass assignments. Even if toponium and Z are practically degenerate, the mixing angle will remain rather small ($|\theta|^2 < 0.01$) since the difference of the widths $\Gamma_Z - \Gamma_V$ is far larger than the off-diagonal element of the mass matrix that characterizes the toponium-Z interaction energy. We shall now present a complete discussion of the formalism and subsequently illustrate our results by calculations performed in the framework of specific potential models.

To describe a reaction $i \to f$ which may either be mediated by Z or toponium exchange,* we start by defining the propagators of the unmixed Z_0 and V_0.

$$= \frac{1}{s - m_{Z_0}^2 + i m_{Z_0}\Gamma_{Z_0}(s)} \qquad (1)$$

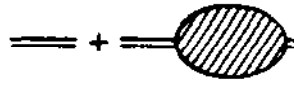

$$= \frac{1}{s - m_{V_0}^2 + i m_{V_0}\Gamma_{V_0}(s)} \,. \qquad (2)$$

The proper self-energy part of the Z_0 propagator is due to fermion loops—including the $t\bar{t}$ continuum in the dispersive part but *not* the toponium state.

* Since narrow toponium states do not overlap, the mixing problem can be treated one by one.

The bare Z_0 mass parameter is therefore to be identified with the conventional value $m_{Z_0} = 94$ GeV. To obtain the correct toponium decay rates for $m_V \neq m_Z$ it is important to take the energy variation in the bare Z_0 width into account

$$m_{Z_0}\Gamma_{Z_0}(s) = \frac{s}{12\pi}\left(\frac{e}{y}\right)^2 \sum_{\substack{\text{leptons}\\ \text{quarks}}} [v_f^2 + a_f^2] \tag{3}$$

where

$$\begin{aligned} v_f &= 2I_3(f) - 4e(f)\sin^2\theta_W \\ a_f &= 2I_3(f) \\ y &= 2\sin 2\theta_W \ . \end{aligned} \tag{4}$$

The sum over all quark species, except t, includes the color degrees of freedom, and a factor $(1 + \alpha_s/\pi)$ may be attached to take account of QCD radiative corrections.

The self-energy part of the V_0 propagator is due to a variety of channels. The bare mass parameter m_{V_0} is—up to small higher order corrections—the bound state energy of top and antitop quark. The *bare* width Γ_{V_0} is defined by the decay rate of toponium *excluding* contributions mediated by the virtual Z_0 (they are taken care of through mixing!). For the dominating 1^{--} resonances the width is given by

$$\Gamma_{V_0} = \Gamma_{ggg} + \Gamma_{\gamma gg} + \Gamma_{\text{SQD}} + \Gamma_{\gamma^*} + \Gamma_{b\bar{b}}^{\text{bare}} + \cdots \ . \tag{5}$$

The first three contributions are unaffected by the mixing,

$$\Gamma_{ggg} = \frac{10}{81}\,\frac{\pi^2 - 9}{\pi}\,\alpha_s^3\,\frac{\Gamma_0}{\alpha^2 e_t^2} \tag{6}$$

$$\Gamma_{\gamma gg} = \frac{36}{5}\,\frac{\alpha e_t^2}{\alpha_s}\,\Gamma_{ggg} \tag{7}$$

$$\Gamma_{\text{SQD}} = 18\,\frac{G_F^2 m_t^5}{192\pi^3}\,f(m_t^2/m_W^2) \tag{8}$$

$$f(\rho = m_t^2/m_W^2) \approx 2\rho^{-4}[6\{\rho + (1-\rho)\log(1-\rho)\} - 3\rho^2 - \rho^3] \,.$$

The fermion-antifermion rates will be affected by the mixing, and they are given by†

$$\Gamma_{\gamma^*} = 3\Gamma_0 + \sum_{q \neq b} 3e_q^2 \Gamma_0 \tag{9}$$

$$\Gamma_{b\bar{b}}^{\text{bare}} = \Gamma_0 \left\{ \frac{1}{3} + \frac{\chi_W}{8\sin^2\theta_W} + \frac{3\chi_W^2}{128\sin^4\theta_W} \right\} \tag{10}$$

$$\chi_W = \frac{m_V^2}{m_W^2} \, \frac{m_W^2 + m_V^2/8}{m_W^2 + m_V^2/4} \,.$$

All quantities have been expressed in terms of the fictitious electromagnetic decay rate

$$\begin{aligned} \Gamma_0 \equiv \Gamma(V_0 \underset{\gamma^*}{\longrightarrow} e^+e^-) &= 4\alpha^2 e_t^2 \, \frac{|R(0)|^2}{m_V^2} \, \left[1 - \frac{16}{3}\,\frac{\alpha_s}{\pi}\right] \\ \alpha_s &= \frac{12\pi}{27\log(m_V/100\,MeV)^2} \,. \end{aligned} \tag{11}$$

Γ_0 will be evaluated later in the context of specific potential models.

For radial excitations the electric dipole transitions have to be included,

$$\Gamma_{E1}(^3S_1 \to \gamma^3P_J) = \frac{4}{3}\,\frac{2J+1}{9}\,\alpha e_t^2 E_\gamma^3 |D_{PS}|^2 \tag{12}$$

where $D_{PS} = \langle R_P | r | R_S \rangle$. The hadronic cascade decay rates $\Gamma(\pi\pi)$ are very small[21,18] and have therefore been neglected in the following calculations.

---

† The contribution from the virtual photon is treated in lowest-order perturbation theory. Since the $V - \gamma$ interaction energy is very small compared to the V mass, this is legitimate and allows us to reduce the mixing problem to the diagonalization of a 2×2 matrix.

The $V - Z$ junctions define the off-diagonal matrix elements of the mass matrix. Their real part provides the leading contribution,

$$\mathrm{Re}\,\delta m^2_{Z_0V_0} = \frac{ev_t}{y}\, m^2_{V_0} f_V \qquad f_V = [3\Gamma_0/4\pi\,\alpha^2 e_t^2 m_V]^{1/2}\,. \tag{13}$$

In order to obtain the correct pattern for interference between contributions from virtual photons, Z, and W exchange, also the absorptive parts of $\delta m^2_{Z_0V_0}$ have to be considered. They arise in third order of the electroweak couplings,

$$\mathrm{Im}\,\delta m^2_{Z_0V_0} =$$

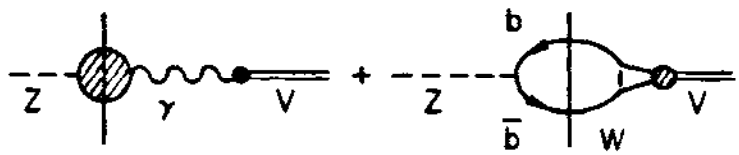

$$= -m_{V_0} \sum_n \sqrt{\Gamma(Z_0 \to n)\,\Gamma(V_0 \to \gamma^*(W) \to n)} \tag{14}$$

with the partial widths as recorded before. The Z width is again to be evaluated for a mass value m_{V_0}. [Note the minus sign.]

Due to the axial part of the neutral current also ${}^3P_1$ states may couple to the Z and decay through the Z. This has been discussed in some detail in Refs. [11, 5]. Although the axial charge a_t is larger than the vector charge v_t, this is by far offset by the smallness of f_A which is of order v/c compared to f_V, making the production rate of 1^{++} states very rare in e^+e^- collisions. Nevertheless, for masses very close to m_Z its dominant decay modes are still mediated by Z. We thus list the relevant formulae and display results for ${}^3P_1$ wherever appropriate,

$$\Gamma({}^3P_1 \to b\bar{b})^{\mathrm{bare}} = \frac{\alpha^2}{2\sin^4\theta_W}\,\frac{|R'_P(0)|^2}{m^4_{A_0}}\,\chi^2_W \tag{15}$$

$$\Gamma({}^3P_1 \to gq\bar{q}) \approx \frac{40}{9\pi}\,\alpha_S^3\,\frac{|R'_P(0)|^2}{m^4_{A_0}}\log\frac{m_{A_0}}{0.6\,GeV} \tag{16}$$

$$\Gamma_{E1}({}^3P_1 \to \gamma\,{}^3S_1) = \frac{4}{9}\,\alpha e_t^2 E_\gamma^3 |D_{SP}|^2 \tag{17}$$

and for the off-diagonal element of the mass matrix

$$\mathrm{Re}\,\delta m^2_{Z_0A_0} = \frac{ea_t}{y}\, m^2_{A_0} f_A \qquad f_A = \left[\frac{72}{\pi}\,\frac{1}{m^5_{A_0}}\,|R'_P(0)|^2\right]^{1/2} . \tag{18}$$

the imaginary part resumes the same general form as in (14).

As a consequence of T invariance the mass matrix is symmetric and finally given by

$$\mathcal{M}^2_0 = \left\| \begin{matrix} m^2_{Z_0} - i m_{Z_0}\Gamma_{Z_0}(s) & \delta m^2_{Z_0V_0} \\ \delta m^2_{V_0Z_0} & m^2_{V_0} - i m_{V_0}\Gamma_{V_0} \end{matrix} \right\| \tag{19}$$

[applicable to P-wave toponia in the same way]. The matrix is diagonalized through a rotation by the complex mixing angle θ

$$\mathcal{M}^2 = C\,\mathcal{M}^2_0 C^{-1} \qquad C = \left\| \begin{matrix} \cos\theta & \sin\theta \\ -\sin\theta & \cos\theta \end{matrix} \right\| \tag{20}$$

with

$$X = \frac{1}{2}\tan 2\theta = \frac{\delta m^2_{V_0Z_0}}{m^2_{Z_0} - m^2_{V_0} - i[m_{Z_0}\Gamma_{Z_0} - m_{V_0}\Gamma_{V_0}]} . \tag{21}$$

The eigenstates of $\mathcal{M}^2$ are no longer orthogonal [for a detailed discussion, see e.g. Ref. [22]].With

$$\begin{aligned} |Z\rangle &= \cos\theta\,|Z_0\rangle + \sin\theta\,|V_0\rangle \qquad \left\langle \tilde{Z}\right| = \cos\theta\,\langle Z_0| + \sin\theta\,\langle V_0| \\ |V\rangle &= -\sin\theta\,|Z_0\rangle + \cos\theta\,|V_0\rangle \qquad \left\langle \tilde{V}\right| = -\sin\theta\,\langle Z_0| + \cos\theta\,\langle V_0| \end{aligned} \tag{22}$$

the scattering amplitude $i \to f$ is conveniently expressed as*

$$\langle f|T|i\rangle = \sum_{a=V,Z} \langle f|a\rangle\, \frac{1}{s - m^2_a + i m_a\Gamma_a}\, \langle \tilde{a}|i\rangle . \tag{23}$$

* For photonic continuum transitions $i \to \gamma \to f$ another term has to be added. The matrix elements $\langle f|V\rangle$ and $\left\langle \tilde{V}|i\right\rangle$ include photonic couplings.

The shift of V and Z masses and widths due to $V-Z$ mixing then follows from

$$[m_V^2 - im_V\Gamma_V] - [m_{V_0}^2 - im_{V_0}\Gamma_{V_0}]$$
$$= \{[m_{Z_0}^2 - im_{Z_0}\Gamma_{Z_0}] - [m_{V_0}^2 - im_{V_0}\Gamma_{V_0}]\}\frac{1}{2}\left[1 - \sqrt{1+4X^2}\right] \tag{24}$$

and a corresponding expression for the intermediate boson with V's and Z's interchanged.

The mixing angle remains small even if the masses of V and Z are completely degenerate as long as $\Gamma_{Z_0} - \Gamma_{V_0}$ is large compared to the off-diagonal element $\delta m^2_{Z_0V_0}/m_{V_0}$. For small θ we may expand Eq. (20) in X^2 (such that the expansion is quadratic in the mixing angle) and the leading terms are given by

$$\frac{1}{2}\left[1 - \sqrt{1+4X^2}\right] = -X^2 + X^4 \ldots \tag{25}$$

If we take as a first estimate $\Gamma_0 \approx 5$ keV for $m_{V_0} = 94$ GeV we find for the $V-Z$ coupling $\delta m^2_{V_0Z_0}/m_{V_0} \approx 0.0014\ m_{V_0}$. The mixing angle is maximal for $m_{V_0} = m_{Z_0}$ but its magnitude $|\theta| \sim 0.05$ remains very small even in this extreme case, so that we might truncate the expansion (25) after the first term. We might also neglect the bare width Γ_{V_0} relative to the Z_0 width which is larger by four orders of magnitude. It is then straightforward to demonstrate that in this approximation all results obtained in the general mixing formalism are equivalent to those in lowest order perturbation theory. In particular the mass shift of the vector meson V resumes the well-known form

$$m_V^2 - m_{V_c}^2 \approx \left[\frac{ev_t}{y} m_{V_0}^2 f_V\right]^2 \frac{m_{V_0}^2 - m_{Z_0}^2}{[m_{V_0}^2 - m_{Z_0}^2]^2 + [m_{Z_0}\Gamma_{Z_0}]^2} \tag{26}$$

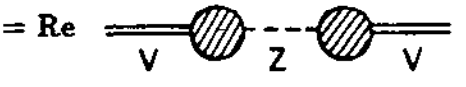

[see also (18)]. The change in the V width from the bare value Γ_{V_0} to Γ_V is dramatic. Taking the imaginary part of $\delta m^2_{Z_0 V_0}$ properly into account, mixing turns on all the channels which are mediated by Z including $\gamma - Z$ interference. To lowest order in θ, however, we rederive again all standard formulae for toponium decays,

$$\Gamma_V - \Gamma_{V_0} \approx \left[\frac{ev_t}{y} m^2_{V_0} f_v\right]^2 \frac{\Gamma_{Z_0}}{[m^2_{V_0} - m^2_{Z_0}]^2 + [m_{Z_0}\Gamma_{Z_0}]^2} \tag{27}$$

$$\approx -\frac{1}{m_{V_0}} \mathrm{Im}$$

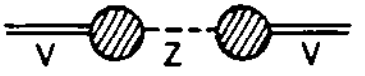

so that finally

$$\Gamma_V = \sum_n \Gamma(V \xrightarrow[\text{dir}]{} n) + \sum_n \Gamma(V \xrightarrow[Z,\gamma,W]{} n) \; .$$

Noticing that the complex rotation angle in this approximation is nothing but the Z propagator times the $V - Z$ coupling constant, we can calculate all $i \to f$ scattering amplitudes up to an accuracy of $O(\theta^2)$ by just applying ordinary lowest-order electroweak perturbation theory as outlined in detail for μ- and quark-pair production in Ref. [6]. For mass and width parameters in the Breit-Wigner form of the V and Z propagators of course the shifted quantities m_V, Γ_V, etc. must be utilized.

2.2 Toponium parameters in potential models.

To present a comprehensive scenario for toponium production in e^+e^- collisions we have evaluated the energy levels, the wave functions $R_S(0)$ and $R'_P(0)$ and the dipole matrix elements of the first 12 S and P wave states for top quark masses between 30 and 60 GeV. To estimate the model dependence we adopted two potentials which both correctly describe charmonium and bottomium spectroscopy but differ if extrapolated into the short-distance regime below 0.1 fm.

The small distance part of both potentials corresponds to a logarithmically softened Coulomb singularity. The more singular choice is represented by Richardson's potential[28]

$$V_R(r) = -\frac{4}{3}\frac{12\pi}{33-2n_F}\int \frac{d^3q}{(2\pi)^3}\,\frac{e^{i\vec{q}\vec{r}}}{q^2\log(1+q^2/\Lambda^2)} \qquad (28)$$
$$n_F = 3 \qquad \Lambda = 398\ MeV\ .$$

As an alternative we have adopted[5] the potential

$$V_T(r) = -\frac{16\pi}{25}\,\frac{1}{rf(r)}\,\left[1+\frac{2\gamma_E+53/75}{f(r)}-\frac{462\log f(r)}{625 f(r)}\right]+a\sqrt{r}+c$$
$$f(r) = \log\left[\frac{1}{(\Lambda_{\overline{MS}}r)^2}+b\right] \qquad \Lambda_{\overline{MS}} = 140\ MeV \qquad (29)$$
$$a = 0.63\ GeV^{3/2}\ ; \quad b = 20\ ; \quad c = -1.39\,GeV$$

which incorporates the asymptotic behavior predicted by a two-loop calculation.[24]

A convenient parametrization of the results is given by

$$E_B = \epsilon_0+\epsilon_1\delta+\epsilon_2\delta^2 \qquad \delta \equiv 1-\frac{m_t}{45\,GeV}$$
$$\Gamma_0 = \gamma_0\left(\frac{m_t}{45\,GeV}\right)^{\gamma_1}[1+\gamma_2\delta+\gamma_3\delta^2]$$
$$R'_P(0)^2/m_A^4 = \rho_0\left(\frac{m_t}{45\,GeV}\right)^{\rho_1}[1+\rho_2\delta+\rho_3\delta^2] \qquad (30)$$
$$\Sigma\Gamma_{E1} = \delta_0\left(\frac{m_t}{45\,GeV}\right)^{\delta_1}[1+\delta_2\delta+\delta_3\delta^2]$$

E_B is the binding energy so that the toponium mass is $m = E_B + 2m_t$. Fits to the coefficients are displayed in Tables 1-4.

Energy levels as well as Γ_0, R'^2_P/m^4 and the couplings f_V and f_A are shown in Figs. 1-3 for the two potentials under discussion. Our results for the lowest

lying levels are in essential agreement with those of Ref. [5]. Evidently a measurement of the energy differences, and particularly of $\Gamma_0(1S)$ would allow us to distinguish clearly between the two cases. In Fig. 4 we compare the effective coupling constants f_V and f_A with another for the lowest lying resonances in the Richardson potential. It is clear that production of P-wave resonances will be less frequent than S-wave production.

Based on the previous estimates and anticipating a quantitative back-up in the following subsection, we present the dominant partial and total decay rates of 1^{--} vector states as a function of m_V in Figs. 5a-7a, and the corresponding branching ratios in Figs. 5b-7b for $1S$, $2S$ and $3S$ states, including the Z decay channels in lowest order perturbation theory. The branching ratio for SQD's becomes particularly large for the higher radial excitations since annihilation decays are of decreasing importance whereas the rate for SQD's is independent of the wave function in the spectator model. This tendency continues to hold for higher radial excitations as discussed in more detail in Refs. [14, 20].

Figures 8 and 9 display the dominant decay rates and branching ratios of axial vector 1^{++} ($^3P_1$) states. Evidently it is only the narrow mass range $m_Z \pm 3$ GeV where Z decays dominate. Outside this band P-state decays are dominated by dipole transitions and SQD's in the low and high mass range respectively.

2.3 Scrutinizing Toponium-Z Mixing.

Armed with the input from potential models we return to the quantitative discussion of the $V - Z$ mixing problem. In Figs. 10a,b the real and imaginary parts of X^2, with $X = \frac{1}{2}\tan 2\theta$ defined in Eq. (21), are presented as a function of the mass values m_V and m_A for 1^3S_1 and 1^3P_1 states. Note that it is $X^2 \approx \theta^2$ and not the mixing angle itself that governs the mass shift and the change in the width of the toponium state. As anticipated, X^2 is less than a percent everywhere.

As outlined above, $V - Z$ mixing leads to an increase of the toponium width and to a shift of the mass. The mass shift for $1S$ toponium is shown in Fig.

11. The maximum value does not exceed 5 MeV. The mass shift is proportional to $f_V^2(\Gamma_0)$ and therefore decreases for higher radial excitations so that the level spacings are affected by electroweak interactions. Also the ${}^1S_0 - {}^3S_1$ hyperfine splitting receives important contributions from electroweak effects. For all practical purposes, however, this mass shift will presumably be buried in the uncertainties of the potential model and in the inaccuracy of the experimental mass determination.

As proved before, lowest order perturbation theory is not complementary to the $Z - V$ mixing formalism but is just the first term of a systematic expansion in the mixing angle θ and Γ_{V_0}/Γ_Z. If the s dependence of Γ_Z and the imaginary part of $\delta m^2_{V_0 Z_0}$ are properly taken into account, the two approaches coincide up to corrections of order θ^2. These amount to less than 10^{-2} $(2 \cdot 10^{-4})$ even in the extreme case of an $S(P)$ state that is nearly degenerate with the Z. This is demonstrated in Figs. 12a,b where we compare the mass shift and shift of the width predicted in the mixing formalism with first order perturbation theory.

Since the mixing angle is so small, the ground state and the radial excitations can be considered separately and the whole toponium system can be treated by a sequence of 2×2 mixing problems below open top threshold.* However, it should be noticed that the mass shifts (that may be positive or negative) and the negative contributions to the Z width act in a cumulative way. Since individual shifts of the Z mass and width are just opposite in sign to those of toponia [as follows readily from Eq. (24) together with its Z analogue], a handy approximation for the Z parameters, valid for V's in the neighborhood of Z, is finally given by

$$M_Z - M_{Z_0} = -\sum_n \left[\frac{ev_t}{y} m^2_{V_{0(n)}} f_{V(n)}\right]^2 \frac{m_{V_{0(n)}} - m_{Z_0}}{[m^2_{V_{0(n)}} - m^2_{Z_0}]^2 + [m_{Z_0}\Gamma_{Z_0}]^2} \quad (31)$$

$$\Gamma_Z - \Gamma_{Z_0} = -\sum_n \left[\frac{ev_t}{y} m^2_{V_{0(n)}} f_{V(n)}\right]^2 \frac{\Gamma_{Z_0}}{[m^2_{V_{0(n)}} - m^2_{Z_0}]^2 + [m_{Z_0}\Gamma_{Z_0}]^2} \quad (32)$$

* Toponium-toponium mixing above threshold, where this simple scheme does not apply anymore, is beyond the scope of the present investigation.

where the notation follows Eqs. (26, 27). The summation is to be carried out over all narrow toponium states below threshold. Note that depending on $m_{V_0(n)} <$ or $> m_{Z_0}$ the contribution to the Z mass shift may be positive or negative. In fig. 13 we therefore show the shift of the Z parameters which is induced by the states below threshold as a function of m_t. Even their cumulative effect remains small. Contributions from open top production on the shift of the Z mass and its width have been estimated in the quark model, based on duality arguments.[25,26] Depending on m_t their effect can be important.

3. TOPONIUM PRODUCTION IN e^+e^- COLLISIONS

The previous discussion of toponium properties was completely general and applies equally well to a resonance produced e.g. in hadronic collisions. However, the only place where we may hope to observe toponium in the near future is resonant e^+e^- production. Some aspects are specific to this case and have to be studied in detail.

(1) The production amplitude for fermion-antifermion final states will receive not only contributions from toponium, but also from the continuum due to virtual Z and photon exchange—as broadly discussed in the preceding section. Although many of the resulting wild interferences will be washed out by the experimental beam energy spread, some remain detectable and may even dominate the behavior of the cross section.

(2) Production rates on and off resonance depend sensitively on the beam polarization and on the kinematics of the final state. [Even for unpolarized beams the resonance will be polarized, and this polarization can be observed in SQD's.]

(3) The forward-backward asymmetries can be remarkably large and quite different on and off resonance.

(4) Transversely polarized e^+e^- beams will induce azimuthal asymmetries.

Just like the total cross section, all these quantities are in general affected by resonance-continuum interference, but the consequences of smearing effects due to the beam energy resolution must be carefully studied. We shall now treat these points in detail.

We have convinced ourselves before that the mixing formalism and lowest order perturbation theory lead to practically identical results. We shall therefore limit the subsequent discussion to the second, intuitively more appealing alternative.

The full amplitude of the reaction $e^+e^- \to f\bar{f}$ is a superposition of γ, Z and toponium exchange. For specified helicities $\frac{1}{2}h_e$, $\frac{1}{2}h_f = \pm\frac{1}{2}$ of the initial and final fermions the amplitude reads after splitting off the fermionic currents, Ref. [6],

$$\begin{aligned}\mathcal{F} &= \frac{e^2 e_e e_f}{s} + \left(\frac{e}{y}\right)^2 \frac{(v_f - h_f a_f)(v_e - h_e a_e)}{s - m_Z^2 + i m_z \Gamma_Z} \\ &\quad + (m_V^2 f_V)^2 \frac{(\lambda_f - h_f \lambda_f')(\lambda_e - h_e \lambda_e')}{s - m_V^2 + i m_V \Gamma_V} \qquad (33) \\ &= \frac{1}{s}\mathcal{F}_B + \frac{(m_V^2 f_V)^2}{s - m_V^2 + i m_V \Gamma_V}\mathcal{F}_R\end{aligned}$$

where

$$\begin{aligned}\lambda_f &= \frac{e^2 e_f e_t}{s} + \left(\frac{e}{y}\right)^2 \frac{v_f v_t}{s - m_Z^2 + i m_Z \Gamma_Z} \\ \lambda_f' &= \qquad\quad + \left(\frac{e}{y}\right)^2 \frac{a_f v_t}{s - m_Z^2 + i m_Z \Gamma_Z}\end{aligned} \qquad (34)$$

and $\lambda_e^{(\prime)}$ correspondingly.

Some of the final states—those from "direct" toponium decays like ggg—have no $\bar{\text{o}}$ counterpart in the continuum. In general, however, and in particular close to the Z, interference effects are very important, and we shall discuss them for the observables listed above.

3.1 The Total Cross Section

Since many of the subsequent arguments apply equally well to the discussion of asymmetries, we shall present the results for the total cross section in detail. The fermion production cross section for unpolarized beams,

$$\sigma(s) = \frac{s}{48\pi} \sum_{h_f h_e} |\mathcal{F}|^2 \,, \tag{35}$$

exhibits a rapid variation in the resonance region. As long as either the photon or the Z dominates, σ varies between a (near) zero* and the unitarity limit

$$\sigma_{\max} = \frac{12\pi}{m_V^2} B(e^+e^-)\, B(f\bar{f}) \,. \tag{36}$$

The precise location of the minimum depends on the relative phases between background and resonance amplitudes. For the photon the interference pattern is destructive below the resonance and constructive above [residue $g_\gamma^2 > 0$],

$$\mathcal{F}[\gamma] \sim \frac{1}{s} + \frac{1}{s}\,\frac{g_\gamma^2}{s - m_V^2}\,\frac{1}{s} \sim 1 + \frac{g_\gamma^2}{s[s - m_V^2]} \tag{37}$$

while in the Z range the interference pattern is just opposite so along as $m_V < m_Z$,

$$\mathcal{F}[Z] \sim 1 + \frac{g_Z^2}{[s - m_Z^2][s - m_V^2]} \,. \tag{38}$$

If photon and Z amplitudes are added, the cross section shifts away a little from the extreme values. Various helicity amplitudes then contribute which approach

* For the photon this phenomenon is well-known from J/ψ production; an exact zero occurs in the complex energy plane by an amount $O(\Gamma)$ away from the real axis, see e.g. Refs. [27]. In the case of Z, the imaginary part of the Z propagator pulls this zero onto the real axis for $m_V \to m_Z$. This point is nicely discussed from the perspective of the mixing formalism in Ref. [28].

their extrema at different energy values. In Fig. 14 we give two examples of the μ-pair cross section in the resonance region corresponding to top quark masses of 40 and 47 GeV. By contrast, those final states which originate from "direct decays" (SQD's and gluons) will exhibit the usual Breit-Wigner resonance enhancement

$$\sigma(\text{direct}) = \frac{12\pi\,\Gamma(ee)\,\Gamma(\text{direct})}{[s - m_V^2]^2 + [m_V\Gamma_V]^2}\,. \tag{39}$$

For a wide range of masses the interference effects will be rendered unobservable once the inherent energy spread of the beams is taken into account which increases with energy in fact. This tendency is already apparent when one moves from J/ψ to Υ. Remnants of the interference effects are still visible in the μ-pair cross section around J/ψ. In the Υ region an incoherent sum of the continuum and the properly smeared resonance is fully adequate. For toponium the same approximation is no longer true, however, once the toponium mass is close to m_Z, as shown previously.[19] In this case the integrated cross section is no longer determined by $\Gamma(ee)$, and the resonance enhancement may even be turned into a dip. This phenomenon is not correlated to the dip in the cross section before smearing. In fact, it is a consequence of the non-real character of the Z background amplitude.

For toponium resonances whose width Γ_V is much smaller than the beam spread δW, the folding of the cross section with the resolution function

$$\langle\sigma(W)\rangle = \int dW'\,r(W - W'/\delta W)\,\sigma(W') \tag{40}$$

can be worked out analytically. The smeared cross section (normalized to the pointlike cross section) can be expressed in the form

$$\begin{aligned}\langle R(W)\rangle &= R_V(f)\{[1 + \rho'(f)]r'(z) + \rho''(f)r''(z)\} + R_{\text{cont}} \\ z &= (W - m_V)/\delta W\,.\end{aligned} \tag{41}$$

R_V is the well-known resonance enhancement if interference effects and radiative

corrections are ignored and a Gaussian beam spread is assumed

$$R_V(f) = \frac{9\pi}{2\alpha^2}\,\frac{\Gamma(ee)\,B(ff)}{\sqrt{2\pi}\,\delta W} \tag{42}$$

$$\Gamma(ff) = \Gamma_0\left(\frac{m_V^2}{e_e e^2}\right)^2 [|\lambda_f|^2 + |\lambda_f'|^2]$$

$$= \Gamma_0\left[1 - \frac{2v_e v_f}{y^2 e_e}\,\mathrm{Re}\,\chi_Z + \frac{v_e^2(v_f^2+1)}{y^4 e_e^2}\,|\chi_Z|^2\right] \tag{43}$$

where $\chi_Z = m_V^2/[m_V^2 - m_Z^2 + im_Z\Gamma_Z]$.

ρ' and ρ'' characterize the interference effects and depend on the final state. [They both vanish for direct decays.] ρ' is non-zero only if the background amplitude is non-real as for Z exchange in the energy range close to the Z mass. In the extreme case of Z dominance discussed in Ref. [19],

$$1 + \rho' = \frac{[m_V^2 - m_V^2]^2 - [m_Z\Gamma_Z]^2}{[m_V^2 - m_Z^2]^2 + [m_Z\Gamma_Z]^2}\ . \tag{44}$$

This coefficient turns the resonance bump into a dip on top of Z. The general case (sum over helicities $h_f, h_e = \pm$)

$$\rho' = b\sum_{h_f h_e}\mathrm{Im}\mathcal{F}_B^*\mathcal{F}_R \Big/ \sum_{h_f h_e}|\mathcal{F}_R|^2 \tag{45}$$

$$b = [|\lambda_e|^2 + |\lambda_e'|^2]/[6\pi\,B(ee)]$$

is shown in Fig. 15a for μ-pair and quark-antiquark pair production. As evident from (44) it is appreciably different from zero only for m_V close to m_Z. Note that ρ' depends on the potential model only through the branching ratio $B(ee)$. $R_V\rho'$ is independent of Γ_V and depends only on $\sqrt{\Gamma(ee)}\,\sqrt{\Gamma(ff)}$.

The second term originates from the interference between the real (antisymmetric) part of the Breit-Wigner amplitude and the continuum,

$$\rho'' = b \sum_{h_f h_e} \mathrm{Re}\, \mathcal{T}_B^* \mathcal{T}_R \Big/ \sum_{h_f h_e} |\mathcal{T}_R|^2 \,. \tag{46}$$

It will be visible as long as $R_V \rho''$ is comparable to R_{cont}. A characteristic example is given by the ψ where $\rho''(\mu) = 2\alpha/3\, B(\mu\mu) \approx 0.07$ is rather small but $R_V \rho''(\mu) = 3\pi\Gamma(ee)/\alpha\sqrt{2\pi}\delta W \approx 2.6$ for $\delta W = 1\, MeV$ is nevertheless of order unity. For a resonance very close to Z, (46) can be simplified to

$$\rho'' = \frac{2\Gamma_Z m_Z (m_V^2 - m_Z^2)}{[m_V^2 - m_Z^2]^2 + [m_Z \Gamma_Z]^2} \,. \tag{47}$$

ρ'' is shown in Fig. 15b for μ-pair and quark-antiquark final states. Since R_V is not much larger than R_{cont} [in fact, it is often even smaller], the asymmetry effect can only be visible if ρ'' is not far from unity. Demanding $\rho'' > 0.2$, i.e., a 10% effect in the shape of the resonance, we are limited to the region $m_V \gtrsim m_Z - 10$ GeV for the toponium mass.

The energy variation of the cross section is relegated to the resolution functions $r'(z)$ and $r''(z)$. These are universal functions determined by the beam characteristics and radiative corrections. In the following we will use a Gaussian shape for r

$$r'(z) = e^{-z^2/2} \tag{48a}$$

and consequently

$$r''(z) = \frac{\mathbf{P}}{\pi} \int \frac{dx}{x} r'(z-x) = \frac{2}{\sqrt{\pi}} Er\, fi\left(\frac{z}{\sqrt{2}}\right) e^{-z^2/2} \,. \tag{48b}$$

However, the same formulae hold true if radiative corrections are taken into account by utilizing[39]

$$r'_{\mathrm{RAD}}(z,t) = \Gamma(1+t)\, e^{-z^2/4} D_{-t}(-z)$$

where $D_\nu(x)$ denotes Weber's parabolic cylinder function.

The effect of the smearing procedure on μ-pair production (and similarly for quark production) is shown in Figs. 16a and 16b for the top quark masses m_t = 40 and 47 GeV.

3.2 Polarization Asymmetry

It has been suggested already before that measurements with polarized beams could provide important information on the electroweak coupling of toponium.[6,7] The polarization asymmetry is defined through

$$\alpha(RL) = \frac{\sigma_R - \sigma_L}{\sigma_R + \sigma_L} \tag{49}$$

where σ_R, σ_L denote the cross section for right-handed, left-handed electrons. Neglecting background channels for the moment we find that on top of the resonance

$$\alpha(\mathrm{RL})^{\mathrm{on}} = -\frac{2\mathrm{Re}(\lambda_e^* \lambda_e')}{|\lambda_e|^2 + |\lambda_e'|^2} \tag{50}$$

The asymmetry is independent of the final state. It is displayed as a function of the toponium mass in Fig. 17 where it is compared with the asymmetry in $\mu^+\mu^-$ production of the continuum. Note that both are strikingly different except in the range very close to Z where the interference with the background amplitude for fermionic final states plays an important role to be discussed now.

The interference pattern for fermionic final states is complex due to the interplay of γ, Z (and even W exchange) in the resonance and background channels. [Not that on and off resonance behavior is identical as long as either γ or Z are dominating.] For perfect energy resolution the dependence of $\alpha(RL)$ on energy and toponium masses is given by

$$\alpha(\mathrm{RL}) = \frac{\sum_{h_f h_e} h_e |\mathcal{F}(h_f, h_e)|^2}{\sum_{h_f h_e} |\mathcal{F}(h_f, h_e)|^2} \,. \tag{51}$$

It varies rapidly around the resonances (Figs. 18a and 18b for m_t = 40 and 47 GeV).

The energy spread demands averaging numerator and denominator of Eq. (51) over the beam profile. The result can be cast into a form analogous to (41),

$$\langle\alpha(\mathrm{RL})\rangle = \frac{[\alpha(\mathrm{RL})^{on} + \alpha(\mathrm{RL})']r'(z) + \alpha(\mathrm{RL})''r''(z) + \alpha(\mathrm{RL})^{off}\eta}{[1+\rho']r'(z) + \rho''r''(z) + \eta} \,. \qquad (52)$$

The auxiliary quantities α' and α'' are fixed by the symmetric and antisymmetric parts of the polarized cross sections

$$\begin{aligned} \alpha(\mathrm{RL})' &= b\sum_{h_f h_e} h_e \mathrm{Im}\mathcal{F}_B^*\mathcal{F}_R \Big/ \sum_{h_f h_e}|\mathcal{F}_R|^2 \\ \alpha(\mathrm{RL})'' &= b\sum_{h_f h_e} h_e \mathrm{Re}\,\mathcal{F}_B^*\mathcal{F}_R \Big/ \sum_{h_f h_e}|\mathcal{F}_R|^2 \end{aligned} \qquad (53)$$

$\eta = R^{\mathrm{cont}}/R_V$ parametrizes the strength of the resonance excitation.[16] In Figs. 19 we display $\alpha(\mathrm{RL})'$ and $\alpha(\mathrm{RL})''$ for μ pairs and quarks in the final state. Below $m_Z - 2\Gamma_Z$ both quantities have a negligible effect on the asymmetry.

In fig. 20a and 20b we finally show how the polarization asymmetry actually looks in the resonance region for $m_t = 40$ and 47 GeV after smearing.

For direct decays of toponia Eq. (52) simplifies considerably since all primed quantities and η vanish.

For unpolarized beams the toponium resonance becomes longitudinally polarized to a degree $\langle\vec{s}_V\vec{n}_e\rangle = \alpha(RL)^{\mathrm{on}}$ which can be measured e.g. in semileptonic SQD's through the forward-backward asymmetry of the emitted leptons.[14]

3.3 Forward-Backward Asymmetries

The angular distribution of the outgoing fermion in $e^+e^- \to f\bar{f}$ for unpolarized beams is of the general form

$$\frac{d\sigma}{d\cos\theta} \propto (1+\cos^2\theta) + \alpha(\mathrm{FB}) \cdot 2\cos\theta \ . \tag{54}$$

The integrated asymmetry between forward and backward hemispheres then follows from

$$\frac{\sigma_F - \sigma_B}{\sigma_F + \sigma_B} = \frac{3}{4}\alpha(\mathrm{FB}) \ . \tag{55}$$

The parameter $\alpha(FB)$ is given by the helicity amplitudes as

$$\alpha(\mathrm{FB}) = \frac{\sum_{h_f h_e} h_f h_e |\mathcal{F}(h_f, h_e)|^2}{\sum_{h_f h_e} |\mathcal{F}(h_f, h_e)|^2} \tag{56}$$

eventually averaged over the beam profile. Inspection of this formula on top of the resonance, with background channels neglected, readily reveals

$$\alpha(\mathrm{FB})_f^{on} = \alpha(\mathrm{RL})_e^{on}\alpha(\mathrm{RL})_f^{on} \tag{57}$$

so that the μ pair FB asymmetry is just the square of the polarization asymmetry.[17] Comparing the asymmetries on and off resonance we find again a striking difference in the energy region below and above the Z, Fig. 21. This dramatic effect, showing up as wild fluctuations in the energy dependence of the FB asymmetry for perfect resolution, Fig. 22, survives even the average over the beam profile. As before,

$$\langle\alpha(FB)\rangle = \frac{[\alpha(\mathrm{FB})^{on} + \alpha(\mathrm{FB})']r'(z) + \alpha(\mathrm{FB})''r''(z) + \alpha(\mathrm{FB})^{off}\eta}{[1+\rho']r'(z) + \rho''r''(z) + \eta} \tag{58}$$

with

$$\alpha(\mathrm{FB})' = b \sum_{h_f h_e} h_f h_e \, \mathrm{Im} \mathcal{F}_B^* \mathcal{F}_R \Big/ \sum_{h_f h_e} |\mathcal{F}_R|^2$$
$$\alpha(\mathrm{FB})'' = b \sum_{h_f h_e} h_f h_e \mathrm{Re} \mathcal{F}_B^* \mathcal{F}_R \Big/ \sum_{h_f h_e} |\mathcal{F}_R|^2 \, . \tag{59}$$

These functions are displayed in Figs. 23 for μ and quark pairs. Both these terms play a minor role for $m_Y \lesssim m_Z - 2\Gamma_Z$. Figure 24 finally demonstrates that for toponium masses in the 80 GeV range FB asymmetries dramatically change in the neighborhood of the resonances even after the beam spread has been averaged over.

3.4 AZIMUTHAL ASYMMETRIES

If the e^+e^- beams are transversely polarized [say e^- along $+x$] the angular distribution of fermion pairs follows from[6]

$$\frac{d\sigma}{d\cos\theta \, d\phi} \propto [1 + \cos^2\theta] + 2\alpha_{\mathrm{FB}} \cos\theta - 2\sin^2\theta [\beta_1 \cos 2\phi + \beta_2 \sin 2\phi] \tag{60}$$

where the coefficients β_1 and β_2 are given by

$$\beta_1 = \frac{\mathrm{Re} \sum_h \mathcal{F}^*(h,h)\mathcal{F}(h,-h)}{\sum_{h_f h_e} |\mathcal{F}(h_f,h_e)|^2}$$
$$\beta_2 = \frac{\mathrm{Im} \sum_h h\mathcal{F}^*(h,h)\mathcal{F}(h,-h)}{\sum_{h_f h_e} |\mathcal{F}(h_f,h_e)|^2} \, . \tag{61}$$

These coefficients are easy to express by the λ couplings on top of the resonance,

$$\beta_1 = \frac{1}{2} \frac{|\lambda_e|^2 - |\lambda_e'|^2}{|\lambda_e|^2 + |\lambda_e'|^2} \qquad \beta_2 = \frac{\mathrm{Im} \lambda_e^* \lambda_e'}{|\lambda_e|^2 + |\lambda_e'|^2} \, . \tag{62}$$

Note that the coefficients are universal for all fermionic final states. This is a consequence of the fact that the reaction proceeds through one state with definite

spin and polarization—similar to the factorization property of the polarization asymmetry. In Figs. 25 the coefficients β_1 and β_2 are plotted and compared with their continuum values off resonance. They are similar in size on and off resonance and for a large mass range equal in sign. β_2 is quite small. And so is β_1 in the 80 GeV mass range. Since the machinery to do the averaging over the beam profile is identical to the previous examples (just exchange the corresponding polarization sums) we won't dwell on these azimuthal asymmetries any longer.

4. HIGHER RADIAL EXCITATIONS

Higher radial excitations will presumably not be used to perform precision measurements of weak couplings or to find new decay modes due to their relatively small production rate and the dominance of SQD's for nearly the whole mass range. Nevertheless, it would be most useful to establish at least the resonance levels and the electronic widths $\Gamma(ee)$ in order to measure the force between heavy quarks at different distances. The flavor independence of the force can be investigated by comparing this result with the potential in charm and bottom quarkonia. To establish the location of the threshold requires a good understanding of the transition between resonance region and open top production. Due to the small level spacing that is comparable to the energy spread of e^+e^- machines, and due to the dominance of SQD's for high radial excitations, open top threshold and the upper part of the resonance region will look rather similar for nearly all top masses as far as magnitude of the smeared cross section and topologies of the final states are concerned.

We start by estimating the heavy quark threshold from charm and bottom production.* Since the hyperfine splitting is expected to be very small between T and T^* we eliminate this effect from the charm and bottom threshold, defining

* We follow closely the discussion of Ref. [30] but incorporate the present information on the B and B^* masses.

average masses

$$m_{\langle D\rangle} = 1.973\ GeV\ , \quad m_{\langle B\rangle} = 5.310\ GeV \tag{63}$$

where $\langle D\rangle = \frac{1}{8}(D^+ + D^0) + \frac{3}{8}(D^{*+} + D^{*0})$ and analogously for B. The average charm (bottom) threshold is thus localized 260 MeV (265 MeV) above $\psi'(\Upsilon'')$. Furthermore, when going from charm through bottom to heavier mesons, the reduced mass

$$\mu(m_Q) = m_q m_Q/(m_q + m_Q) \tag{64}$$

increases to the limiting value of the light quark constituent mass m_q, and this results in a slightly stronger binding. A simple estimate of this effect is based on the logarithmic potential

$$V(r) = c\log r\ ; \quad c = 0.733\ GeV\ . \tag{65}$$

With increasing mass the energy decreases by

$$E(\mu_1) - E(\mu_2) = -\frac{1}{2}c\log\frac{\mu_1}{\mu_2} \tag{66}$$

which leads to a reduction for the threshold of T mesons by

$$2[m_{\langle T\rangle} - m_t] - 2[m_{\langle D\rangle} - m_c] = -c\log\frac{1 + m_q/m_c}{1 + m_q/m_t} \approx -140\ MeV\ . \tag{67}$$

For bottom the reduction amounts to 40 MeV only. The heavy meson threshold is thus located at

$$W_T^{\rm ths} = m_{\Psi'} + 2(m_t - m_c) + 120\,MeV \tag{68a}$$

if we take the charm sector as a guide, or at

$$W_T^{\rm ths} = m_{\Upsilon''} + 2(m_t - m_b) + 225\,MeV \tag{68b}$$

if we rely on $b\bar{b}$. These results hold true for any potential model in as much as it agrees approximately with the log potential in the long range $O(1\,fm)$ part. To

relate these numbers to the Richardson potential we adopt the calculated values for the corresponding binding energies

$$E_B(\Psi') = 702\ MeV \qquad E_B(\Upsilon'') = 572\ MeV$$

and find a remarkable agreement between the predictions from $c\bar{c}$ and $b\bar{b}$,

$$W_T^{\rm ths} = 822\ MeV \quad \text{and} \quad 792\ MeV\ ,$$

respectively. [The corresponding values for V_T turn out to be 16 MeV and 57 MeV, respectively.] Since all corrections are smaller for bottom quarks, those estimates should be less subject to uncertainties, and we have based all our further calculations on a threshold energy of 800 MeV. The number of S states is thus found to rise from 9 at $m_t = 30$ GeV up to 12 at 60 GeV, as indicated in Fig. 1.

In Fig. 26 we show that the suitably averaged [$\delta W = 60$ MeV] S-wave resonance cross section is approximately dual to the cross section for t-quark production once the α_S correction is taken into account. The correction factor to the parton result $3e_t^2$ [γ^* exchange only] is well approximated by

$$\begin{aligned} r_V &= \frac{v(3-v^2)}{2}\ \left\{1 + \frac{4}{3}\alpha_s\left[\frac{\pi}{2v} - \frac{(3+v)}{4}\left(\frac{\pi}{2} - \frac{3}{4\pi}\right)\right]\right\} \\ \alpha_s &= 12\pi/25 \log\left[\frac{vm_t}{\sqrt{1-v^2}}/200\ MeV\right]^2 \end{aligned} \tag{69}$$

(adapted from Ref. [31].)The latter comes already quite close to the (massless) parton result, also shown in Fig. 26. The threshold suppression factor v is largely offset by QCD corrections.* The hadronic widths of resonances above threshold has been estimated to rise significantly to O(100 MeV) or even more with

* It is also important to take these QCD corrections into account for estimates of the electronic width of toponia.

increasing quark mass.[92] Hence their decay properties are essentially unaffected by $V - Z$ mixing. Since these widths are even comparable to the level spacings, no well separable resonances may exist above threshold—even before the beam spread smoothes any resonance structures. We therefore expect the quark model to approximate the cross section for top production sufficiently well above threshold and to join even smoothly to the resonance region.

The rate for SQD's is independent of the wave function whereas the rates for all competing modes decrease with increasing radial quantum number. Thus SQD's dominate for high radial excitations. Not only the total cross section, but also the event properties will therefore essentially be the same above and below threshold. Only in a very narrow range ($m_Z \pm$ 5 GeV) will Z mediated decays be expected to dominate even for the highest radial excitations.

In Figs. 27 and 28 [see Ref. [20]] we show four characteristic cases with representative mass values of 30, 40, 47 and 55 GeV. [The resonant cross sections and the branching ratios are calculated with a lightly different set of input parameters, $E_T^{\rm ths}$ = 780 MeV, no dipole transitions and QCD corrections; this is irrelevant for the present purpose.] Note the large negative contribution to the fermion-antifermion cross section for $\sqrt{s}$ = 94 GeV as a consequence of large destructive interferences.[19] The complete vector and axial-vector contributions to the quark cross sections are given by

$$R_V = 3\,e_t^2\,r_V^{\gamma+Z} r_V \qquad R_A = 3 r_A^Z r_A \tag{70}$$

where r_V is defined in Eq. (69),

$$r_A = v^3\left\{1 + \frac{4}{3}\,\alpha_s\left[\frac{\pi}{2v} - \left(\frac{10}{19} - \frac{22}{5}\,v + \frac{7}{2}\,v^2\right)\left(\frac{\pi}{2} - \frac{3}{4\pi}\right)\right]\right\} \tag{71}$$

and

$$r_V^{\gamma+Z} = (s/4\pi\alpha e_t)^2 |\lambda_e|^2 \tag{72a}$$

$$r_A^Z = (s/4\pi\alpha)^2 |\lambda_c'|^2 \ . \qquad (72b)$$

The axial vector contribution to the continuum, shown separately in Figs. 27 and 28, is quite small throughout the threshold region. The v^3 threshold suppression is by far not compensated by the QCD corrections.[26] Below threshold the quark model correctly reproduces the order of magnitude of the P-wave resonance excitations which are suppressed by more than an order of magnitude relative to the S waves.

5. A Fourth Generation

It is conceivable that another generation of quarks appears in the mass range up to 200 GeV which is expected to be spanned by LEP. Since our formalism applies to quarkonium close to and far from Z, we list the modifications in the electroweak couplings and discuss the resulting alterations if a heavy bottom type quark $\hat{b}$ would exist in this energy range. Apart from a reduction of the dipole rates by a factor of four and a redefinition of Γ_0 by

$$\Gamma_0(\hat{b}) = \Gamma_0(t)/4$$

only the electroweak couplings are affected,

$$v(\hat{b}) = -1 + 4/3 \sin^2\theta_W \qquad a(\hat{b}) = -1$$

$$\lambda_f(\hat{b}) = \frac{e^2 e_f e(\hat{b})}{s} + \left(\frac{e}{y}\right)^2 \frac{v_f v(\hat{b})}{s - m_Z^2 + i m_Z \Gamma_Z}$$

$$\lambda_f'(\hat{b}) = \left(\frac{e}{y}\right)^2 \frac{a_f a(\hat{b})}{s - m_Z^2 + i m_z \Gamma_Z} \ .$$

Assuming small generalized Cabibbo angles there will be no W exchange contribution to $f\bar{f}$ decays. Decays of a heavy bottom system will differ essentially in two aspects from the toponium results:

(a) If its mass were close to m_Z, its decay rates, the effects on the Z mass shift and the changes in the cross sections would be enhanced by a factor $|v(\widehat{b})/v(t)|^2 = 2.8$ so that its width would be comparable to the energy spread of LEP. Also the effects on the Z mass would become noticeable.

(b) If the mass is sufficiently far above the Z, its width will be far smaller than that of a toponium state of the same mass since SQD's are strongly suppressed. Whether they would still constitute an important decay mode depends sensitively on mass and mixing angles of $\widehat{b}$. Their presence or absence could thus provide significant information on the mixing angles.[7] If we take for illustration a state with a mass of 150 GeV and a rate for annihilation decays of 50 keV and if we assume that SQD's could be detected down to a branching ratio of 10%, a Cabibbo suppression factor down to a level of $2 \cdot 10^{-3}$ would be accessible experimentally.

6. CONCLUSIONS

We have developed the toponium-Z mixing formalism in a way that is applicable to arbitrary toponium masses. The results are illustrated by numerical calculations based on two QCD inspired potentials. They are presented in the form of mass dependent parametrizations that can also be used easily for other purposes. We prove that the predictions of the mixing formalism coincide to better than 1% with simple lowest order perturbation theory if the input parameters, wave functions and coupling constants, are derived from generally accepted potential models. The feedback of the mixing on the mass and width of Z is small.

For e^+e^- collisions interesting interference effects are expected between the resonance and the continuum contributions. In particular for a toponium state very close to Z these interference effects are extremely important; they may turn the toponium resonance bump into a dip on top of the Z, as briefly pointed out before. For masses farther away from m_Z, a combined analysis of γ, Z and toponium contributions is required, and we have given analytical expressions for

both the pure and the energy smeared cross sections. Similarly we have derived convenient forms for polarization, forward-backward and azimuthal asymmetries.

Radial excitations below the threshold of open top production will be quite difficult to discriminate against resonances in the continuum since properly smeared production cross sections and final state topologies closely resemble each other.

The results can also be easily applied to quarkonium states formed out of bottom type quarks by using the rules given in the last section. For such a system production and decay properties would be very different from the standard toponium.

When writing up the final form of this paper we received preprints by P. Franzini *et al.*[28] and L. Hall *et al.*[33] where the toponium-Z mixing formalism is considered for V very close to Z. The latter paper and that of M. Chaichian *et al.*[34] emphasizes the virtue of enhanced toponium production near Z for the Higgs search.

ACKNOWLEDGEMENTS

We should like to thank W. Buchmüller and A. Martin for instructive discussions on toponium physics. J.H.K. is grateful to G. Coignet, F. Richard and H. Takek for valuable information on experimental aspects. P.M.Z. acknowledges several discussions with P. Franzini and F. Gilman on the results presented in their paper, and helpful comments by B. Ward. He also thanks S. Brodsky and S. Drell for the warm hospitality extended to him in the SLAC Theory Group. Partial support by SLAC and DFG is gratefully acknowledged.

REFERENCES

1. G. Arnison *et al.*, Phys. Lett. 147B (1984) 493.
2. J. Ellis and M. K. Gaillard, CERN Yellow Reports 76-18 (1976) and 79-01 (1979).
3. K. Fujikawa, Prog. Theor. Phys. 61 (1979) 1186.
4. F. M. Renard, Z. Phys. C1 (1978) 225.
5. J. H. Kühn and S. Ono, Z. Phys. C21 (1984) 395; (E) C24 (1984) 404.
6. L. M. Sehgal and P. M. Zerwas, Nucl. Phys. B183 (1981) 417.
7. J. H. Kühn, Acta Phys. Polon. B12 (1981) 374.
8. S. Pakvasa *et al.*, Phys. Rev. D20 (1979) 2862.
9. G. Goggi and G. Penso, Nucl. Phys. B165 (1980) 429.
10. I. Y. Bigi, J. H. Kühn and H. Schneider, Munich preprint MPI-PAE/PTh 28/78 (1978).
11. J. Kaplan and J. H. Kühn, Phys. Lett. 78B (1979) 252.
12. R. Koniuk *et al.*, Phys. Rev. D17 (1979) 2915.
13. R. Budny, Phys. Rev. D20 (1979) 2763.
14. J. H. Kühn and K. H. Streng, Nucl. Phys. B198 (1980) 71.
15. J. H. Kühn, Acta Phys. Austriaca, Suppl. XXIV (1982) 23.
16. L. M. Sehgal, Proc. 1983 Europhysics Study Conference on Electroweak Effects at High Energies, Erice.
17. A. Martin, International School of Subnuclear Physics, Erice 1984.
18. E. Eichten, SLAC Summer Institute 1984.
19. J. H. Kühn and P. M. Zerwas, preprint CERN-TH 4089/85 (1985), Phys. Lett. B in print.

20. S. Güsken, J. H. Kühn and P. M. Zerwas, preprint CERN-TH 4106/85 (1985), Phys. Lett. B in print.

21. Y. P. Kuang and T. M. Yan, Phys. Rev. D24 (1981) 2874.

22. M. Gourdin, F. M. Renard and L. Stodolsky, Phys. Lett. 30B (1969) 347; L. Stodolsky, Phys. Rev. D1 (1970) 2683.

23. J. L. Richardson, Phys. Lett. 82B (1979) 272.

24. W. Buchmüller and S.-H. Tye, Phys. Rev. D24 (1981) 132.

25. T. H. Chang, K.J.F. Gaemers and W. L. Van Neerven, Nucl. Phys. B202 (1982) 407 .

26. J. Jersak, E. Laermann and P. M. Zerwas, Phys. Rev. D25 (1982) 1218.

27. SLAC Theory Workshop on Ψ, SLAC-PUB-1515.

28. P. J. Franzini and F. J. Gilman, SLAC-PUB-3541.

29. D. Jackson and L. Scharre, Nucl. Inst. and Meth. 128 (1975) 13.

30. C. Quigg and J. L. Rosner, Phys. Rep. C56 (1979) 167.

31. J. Schwinger, Particles, Sources and Fields, II (1973).

32. S. Ono, Z. Phys. C8 (1981) 7.

33. L. J. Hall, S. F. King and S. R. Sharpe, Harvard Preprint HUTP-85/A012.

34. M. Chaichian and M. Hayashi, SLAC-PUB-3549.

Table 1. Parameters of fits to the S- and P- wave energy levels, the fictitious width Γ_0 for S-waves and the strength of P-wave couplings at the origin for the Richardson potential.

	Energy Levels [GeV]			Γ_0 [keV]			
	ϵ_0	ϵ_1	ϵ_2	γ_0	γ_1	γ_2	γ_3
1S	−1.584	.908	.148	7.713	.225	−.118	.014
2S	−.628	.492	.188	2.025	−.017	−.177	.029
3S	−.263	.403	.165	1.091	.062	.066	.134
4S	−.037	.352	.052	.763	.249	.376	.357
5S	.128	.379	.199	.604	−.059	.127	.169
6S	.266	.387	.215	.514	.001	.245	.219
7S	.385	.400	.230	.452	−.118	.162	.184
8S	.491	.415	.245	.411	−.164	.145	.157
9S	.589	.432	.261	.380	−.280	.045	.083
10S	.679	.448	.276	.359	−.298	.013	.095
11S	.764	.467	.299	.337	−.193	−.153	−.146
12S	.895	.485	.304	.319	−.200	.170	.147
	Energy Levels [GeV]			$R'_P(0)^2/m_A^4$ [keV]			
	ϵ_0	ϵ_1	ϵ_2	ρ_0	ρ_1	ρ_2	ρ_3
1P	−.725	.501	.164	23.96	−.939	−.488	.036
2P	−.324	.400	.152	16.57	−1.359	−.716	.036
3P	−.085	.373	.172	12.95	−1.020	−.240	.079
4P	.089	.370	.193	11.05	−.848	.048	.195
5P	.231	.377	.206	9.92	−.666	.332	.371
6P	.353	.390	.222	9.19	−.795	.240	.347
7P	.462	.405	.237	8.64	−1.530	−.484	.115
8P	.561	.422	.252	8.30	−1.535	−.425	.013
9P	.653	.438	.268	8.08	−1.476	−.353	.019
10P	.739	.456	.282	7.86	−1.101	.029	.227
11P	.820	.475	.295	7.67	−1.615	−.457	.050
12P	.897	.493	.310	7.50	−1.213	−.014	.132

Table 2. Same parameters as in Table 1 for V_T potential.

	Energy Levels [GeV]			Γ_0 [keV]			
	ϵ_0	ϵ_1	ϵ_2	γ_0	γ_1	γ_2	γ_3
1S	−1.946	.589	.160	4.066	.060	−.233	.035
2S	−1.278	.390	.164	1.311	−.063	−.028	.146
3S	−.968	.373	.190	.831	−.123	−.038	.108
4S	−.752	.378	.200	.630	−.170	.026	.099
5S	−.582	.386	.208	.514	−.241	−.020	.034
6S	−.441	.395	.215	.438	−.266	−.031	.032
7S	−.320	.404	.222	.384	−.248	.001	.056
8S	−.212	.413	.229	.345	−.224	.031	.064
9S	−.116	.422	.236	.313	−.312	−.055	.032
10S	−.027	.429	.244	.294	−.200	.039	.141
	Energy Levels [GeV]			$R'_P(0)^2/m_A^4$ [keV]			
	ϵ_0	ϵ_1	ϵ_2	ρ_0	ρ_1	ρ_2	ρ_3
1P	−1.367	.372	.157	10.04	−.994	−.187	.240
2P	−1.039	.363	.230	8.79	−1.390	−.396	.109
3P	−.806	.363	.191	7.91	−1.171	−.082	.154
4P	−.629	.374	.201	7.23	−1.398	−.274	.077
5P	−.482	.384	.209	6.70	−.731	.454	.495
6P	−.356	.394	.217	6.26	−.794	.407	.477
7P	−.246	.404	.224	5.92	−1.019	.182	.255
8P	−.147	.414	.231	5.64	−1.176	.029	.153
9P	−.057	.432	.284	5.45	−2.867	−1.683	.712
10P	.027	.434	.249	5.21	−.800	−.521	.608

Table 3. Fit parameters of E1 decays nS(nP) $\to \gamma +\ldots$ for the Richardson potential. [The error of these fits is $\sim 10\%$].

	Γ_{E1} [keV]					Γ_{E1} [keV]			
	δ_0	δ_1	δ_2	δ_3		δ_0	δ_1	δ_2	δ_3
1S	–	–	–	–	1P	50.85	−.793	−.638	.006
2S	1.018	−.189	.836	.806	2P	26.58	.511	.878	1.207
3S	.940	−1.093	.092	−.096	3P	18.66	−4.131	−3.904	5.374
4S	1.586	−.746	.233	1.875	4P	14.18	.880	1.448	1.677
5S	2.280	−7.428	−9.077	24.65	5P	11.81	2.062	3.060	4.961
6S	1.539	1.711	2.419	6.875	6P	10.98	−.629	.137	−.242
7S	1.152	−.837	.651	.980	7P	10.43	−5.115	−4.706	7.672
8S	1.339	−6.925	−6.044	12.09	8P	9.572	−1.541	−.845	.087
9S	1.560	1.018	2.697	4.732	9P	9.054	−4.026	−3.619	4.852
10S	1.949	−5.138	−3.218	1.306	10P	8.963	−4.192	−4.028	6.068

Table 4. Same parameters as in Table 3 for V_T potential.

	Γ_{E1} [keV]					Γ_{E1} [keV]			
	δ_0	δ_1	δ_2	δ_3		δ_0	δ_1	δ_2	δ_3
1S	–	–	–	–	1P	24.50	−.119	.306	.440
2S	.958	−1.330	.307	.283	2P	15.53	−.507	.096	.550
3S	1.329	−.321	1.267	1.419	3P	11.91	−.637	−.048	.048
4S	1.666	−4.486	−3.239	3.681	4P	9.978	.493	1.201	1.074
5S	1.539	−2.814	−1.502	.764	5P	8.600	−1.328	−.703	.020
6S	1.509	−.639	.729	.863	6P	7.775	−1.421	−.766	.066
7S	1.511	−.853	.454	.651	7P	7.029	−.191	.530	.550
8S	1.580	−1.400	−1.494	.010	8P	6.364	−.054	.656	.543
9S	1.566	−.845	.362	.457	9P	5.883	−2.595	−1.920	1.060
10S	1.557	−2.321	−1.118	.512	10P	5.897	−1.905	−1.301	.511

FIGURE CAPTIONS

1. Energy levels of S-wave and P-wave toponia as a function of the top quark mass m_t for (a) the Richardson potential and (b) the V_T potential. The physical threshold for open top hadron production is indicated by a dotted line.

2. The fictitious electromagnetic decay rate Γ_0 [Eq. (11)], parametrizing the quark wave function for S waves at the origin, as a function of the toponium mass for the Richardson potential and the V_T potential.

3. Derivative of the quark wave function for P waves at the origin, determining the strength of toponium couplings to axial vector currents, as a function of the toponium mass. (a) Richardson, (b) V_T potential.

4. Comparison of the effective vector (a) with the axial vector coupling constants (b) to the corresponding quark currents.

5. Total and partial widths of the main decay modes of $1S$ toponium as a function of the toponium mass; branching ratios.

6. Same as Fig. 5, for $2S$ states.

7. Same as Fig. 5, for $3S$ states.

8. Total and partial widths of the main decay modes of $1P$ toponium as a function of the toponium mass.

9. Branching ratios of the main decay modes of $1P$ toponium as a function of the toponium mass.

10. Toponium-Z mixing parameter X^2 as a function of the toponium mass for (a) $1S$ and (b) $1P$ states.

11. Mass shift δm_V of the toponium $1S$ state due to mixing with Z, as a function of the toponium mass.

12. (a) Comparison of the mass shift of $1S$ toponia in the mixing formalism with the lowest order approximation.

(b) The same for the total widths. Γ (lowest order) is the sum of the bare toponium width plus the decays mediated by Z (interference terms included); this is just the result of a naive calculation of the toponium width.

13. Shift of the Z mass (a) and the Z width (b) due to all *narrow* toponium states for a given top quark mass.

14. (a) $R(\mu^+\mu^-)$ for a top quark mass of 40 GeV, (b) for 47 GeV; the sequence of S and P waves is clearly visible in (b). [The cross sections are not yet averaged over the beam profile.]

15. The coefficients (a) $1+\rho'$ and (b) ρ'' in the cross section averaged over the beam spread. They are given as a function of the toponium mass. [ρ' is *very* weakly dependent on the fermion species in the final state.]

16. (a) $\langle R(\mu^+\mu^-)\rangle$ for a top quark mass of 40 GeV, and (b) 47 GeV, averaged over the beam profile with a spread of 32 MeV and 48 MeV, respectively.

17. The polarization asymmetry α(RL) on top of an S-wave toponium resonance as a function of the toponium mass, compared with the corresponding value of the $\mu^+\mu^-$ continuum.

18. Polarization asymmetry α(RL) for a top quark mass of (a) 40 GeV and (b) 47 GeV. For P waves the polarization effect is small.

19. The parameters (a) $\alpha(\mathrm{RL})'$ and (b) $\alpha(\mathrm{RL})''$ in the polarization asymmetry averaged over the beam energy spread as a function of the toponium mass.

20. Polarization asymmetry $\langle\alpha(\mathrm{RL})\rangle$ in μ-pair production averaged over the beam profile for top quark masses (a) 40 GeV and (b) 47 GeV.

21. μ^- forward-backward asymmetry α(FB) on top of an S-wave toponium resonance decaying into $\mu^-\mu^+$, compared with the continuum.

22. μ^- forward-backward asymmetry for a top quark mass of (a) 40 GeV and (b) 47 GeV. S and P-wave resonances behave very differently.

23. The parameters (a) $\alpha(\mathrm{FB})'$ and (b) $\alpha(\mathrm{FB})''$ in the forward-backward asymmetry averaged over the beam energy spread as a function of the toponium mass.

24. μ^- forward-backward asymmetry $\langle\alpha(\mathrm{FB})\rangle$ averaged over the beam profile for top quark masses (a) 40 GeV and (b) 47 GeV.

25. Azimuthal asymmetries β_1 and β_2 on top of an S-wave toponium resonance decaying to $\mu^+\mu^-$, compared with continuum.

26. Comparison of toponium S-wave excitation in the threshold region [smeared over a Gaussian distribution] with the QCD corrected elementary parton term of the continuum $3e_t^2 r_V$, for a top quark mass of 40 GeV.

27. Threshold behavior of toponium and open top production. The dashed area indicates the fraction of SQD events. The contribution from the axial-vector current is indicated by the dotted area. (a) $2m_t = 60$ GeV, (b) $2m_t = 80$ GeV. The dashed line corresponds to the (massless) parton term.

28. Same as Figs. 27 for (a) $2m_t = 94$ GeV and (b) $2m_t = 110$ GeV. The (lower) solid line in (b) characterizes the change of the fermion-antifermion cross section alone.

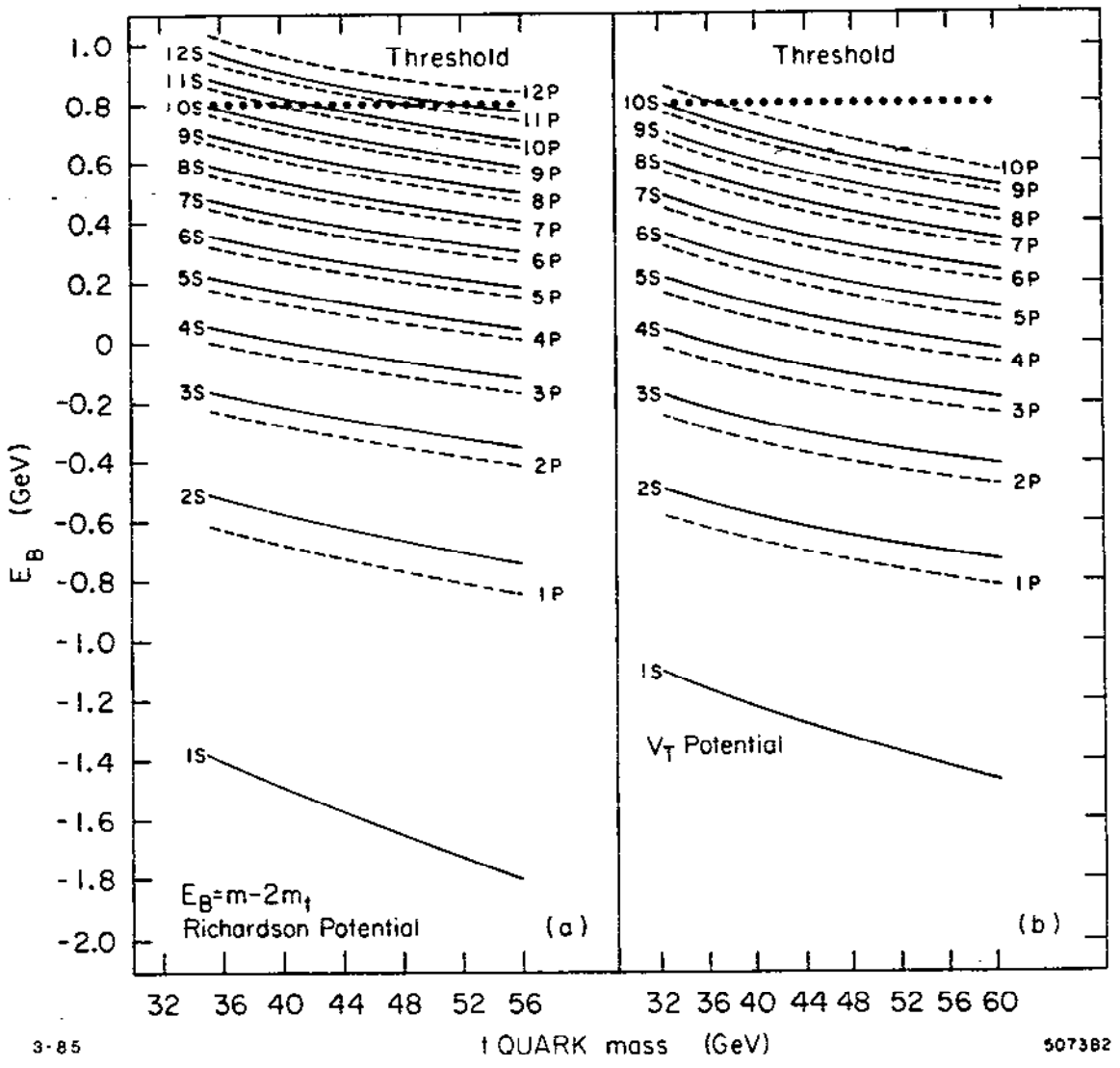
Threshold
12S
11S
10S
9S
8S
7S
6S
5S
4S
3S
2S
1S
12P
11P
10P
9P
8P
7P
6P
5P
4P
3P
2P
1P
E_B (GeV)
E_B=m−2m$_t$
Richardson Potential
(a)
Threshold
V_T Potential
(b)
t QUARK mass (GeV)
3-85
507382

Fig. 1

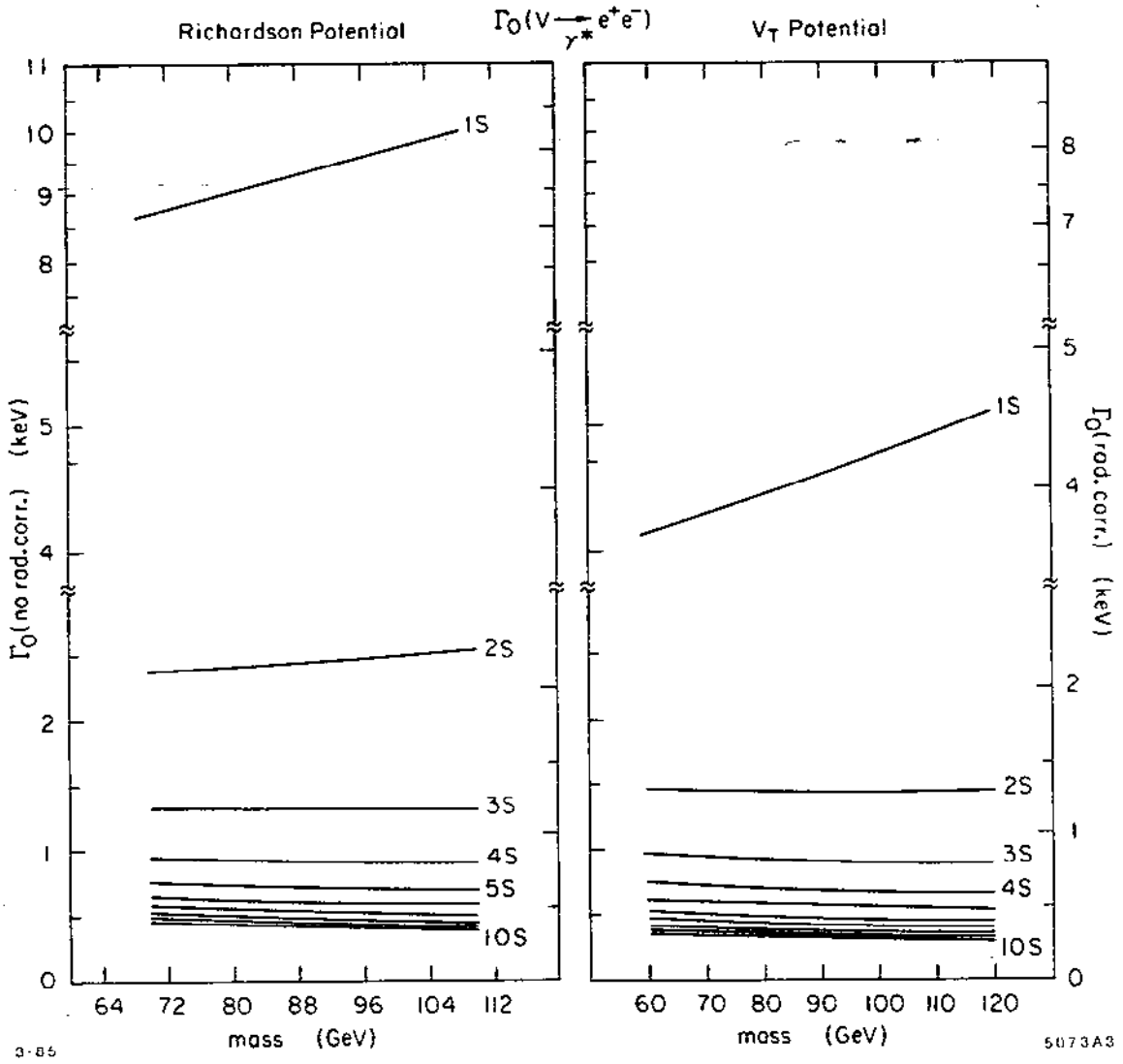
Richardson Potential
$\Gamma_0(V \xrightarrow{\gamma^*} e^+e^-)$
V_T Potential
Γ_0(no rad.corr.) (keV)
Γ_0(rad.corr.) (keV)
1S
2S
3S
4S
5S
10S
mass (GeV)
64 72 80 88 96 104 112
60 70 80 90 100 110 120
3-85
5073A3

Fig. 2

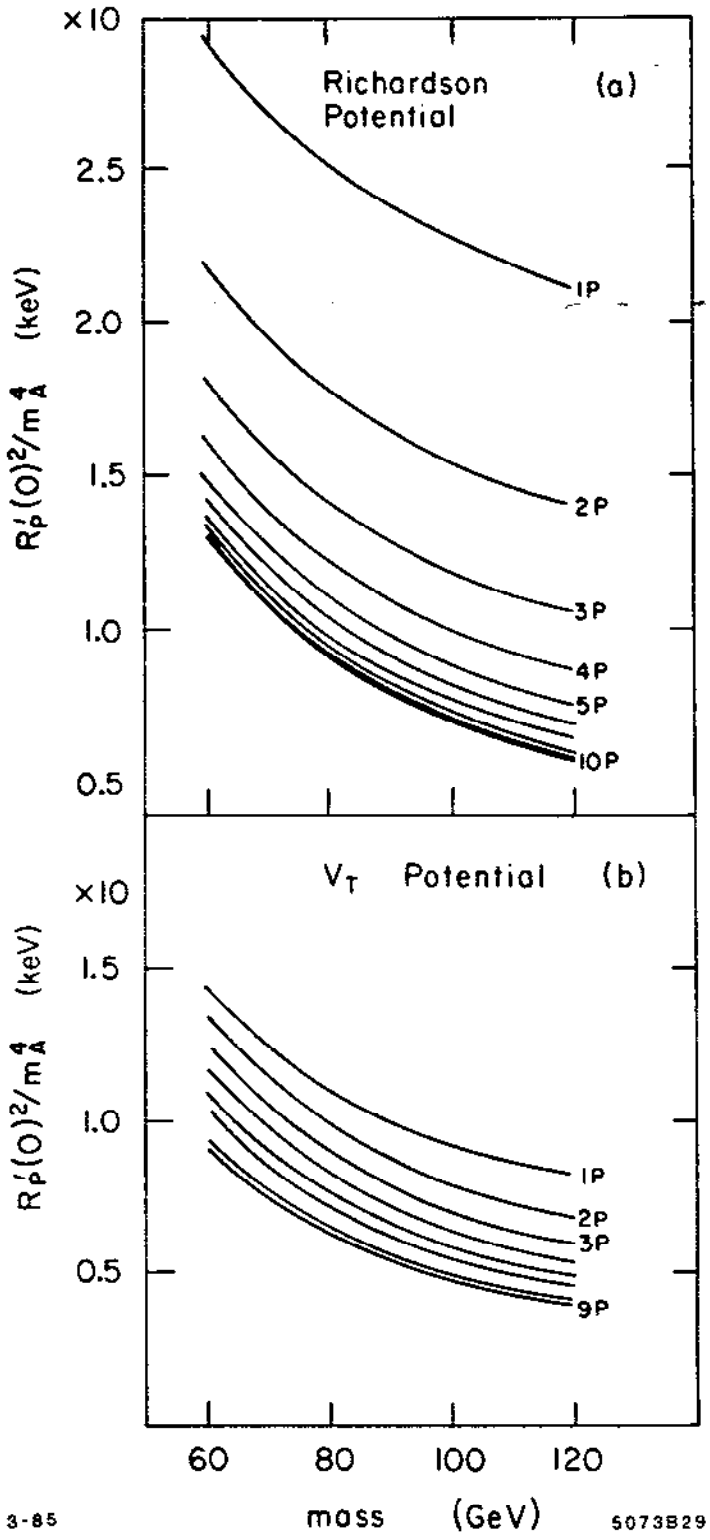
x10
Richardson Potential
(a)
2.5
2.0
1.5
1.0
0.5
$R_p'(0)^2/m_A^4$ (keV)
1P
2P
3P
4P
5P
10P
x10
V_T Potential
(b)
1.5
1.0
0.5
$R_p'(0)^2/m_A^4$ (keV)
1P
2P
3P
9P
60
80
100
120
mass (GeV)
3-85
5073B29

Fig. 3

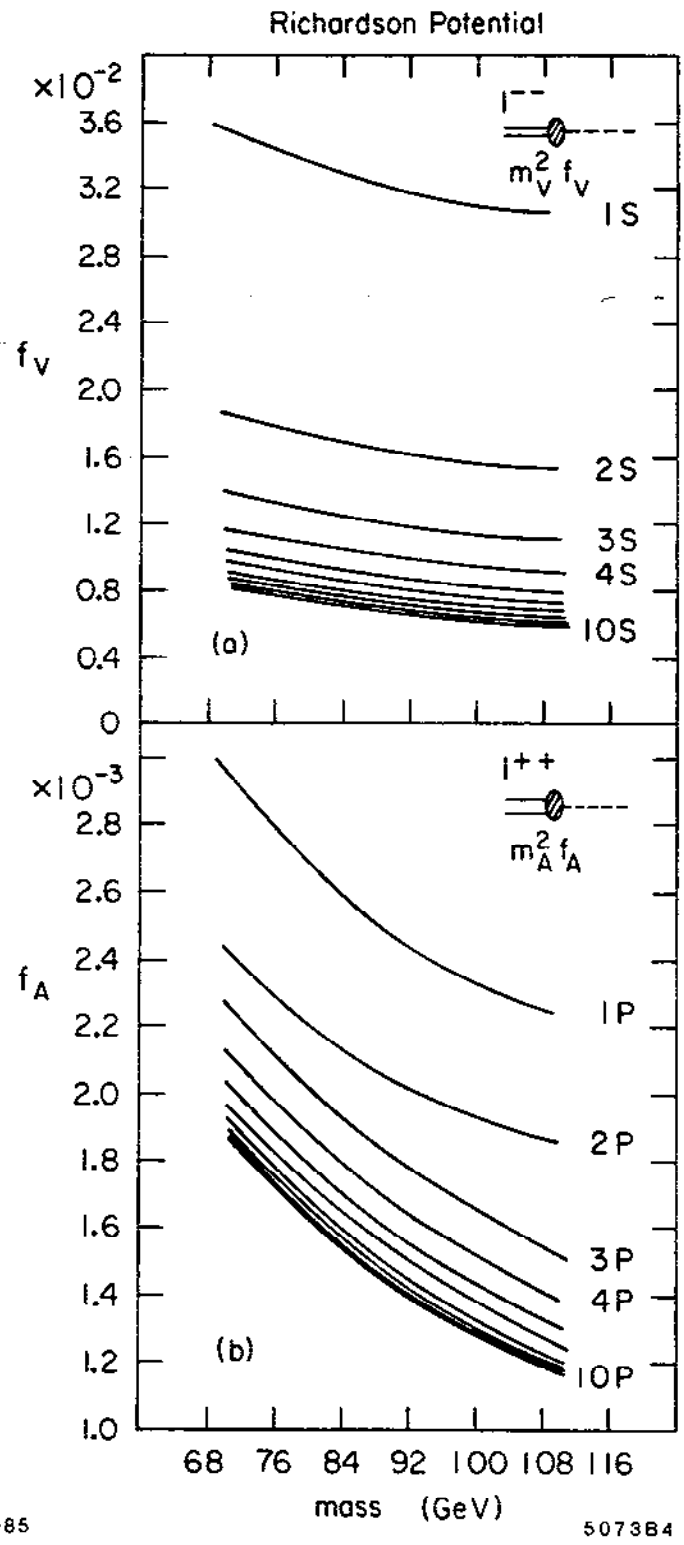
Richardson Potential
×10⁻²
3.6
3.2
2.8
2.4
f_V
2.0
1.6
1.2
0.8
0.4
0
1⁻⁻
m_V² f_V
1S
2S
3S
4S
10S
(a)
×10⁻³
2.8
2.6
2.4
f_A
2.2
2.0
1.8
1.6
1.4
1.2
1.0
1⁺⁺
m_A² f_A
1P
2P
3P
4P
10P
(b)
68 76 84 92 100 108 116
mass (GeV)
3-85
507384

Fig. 4

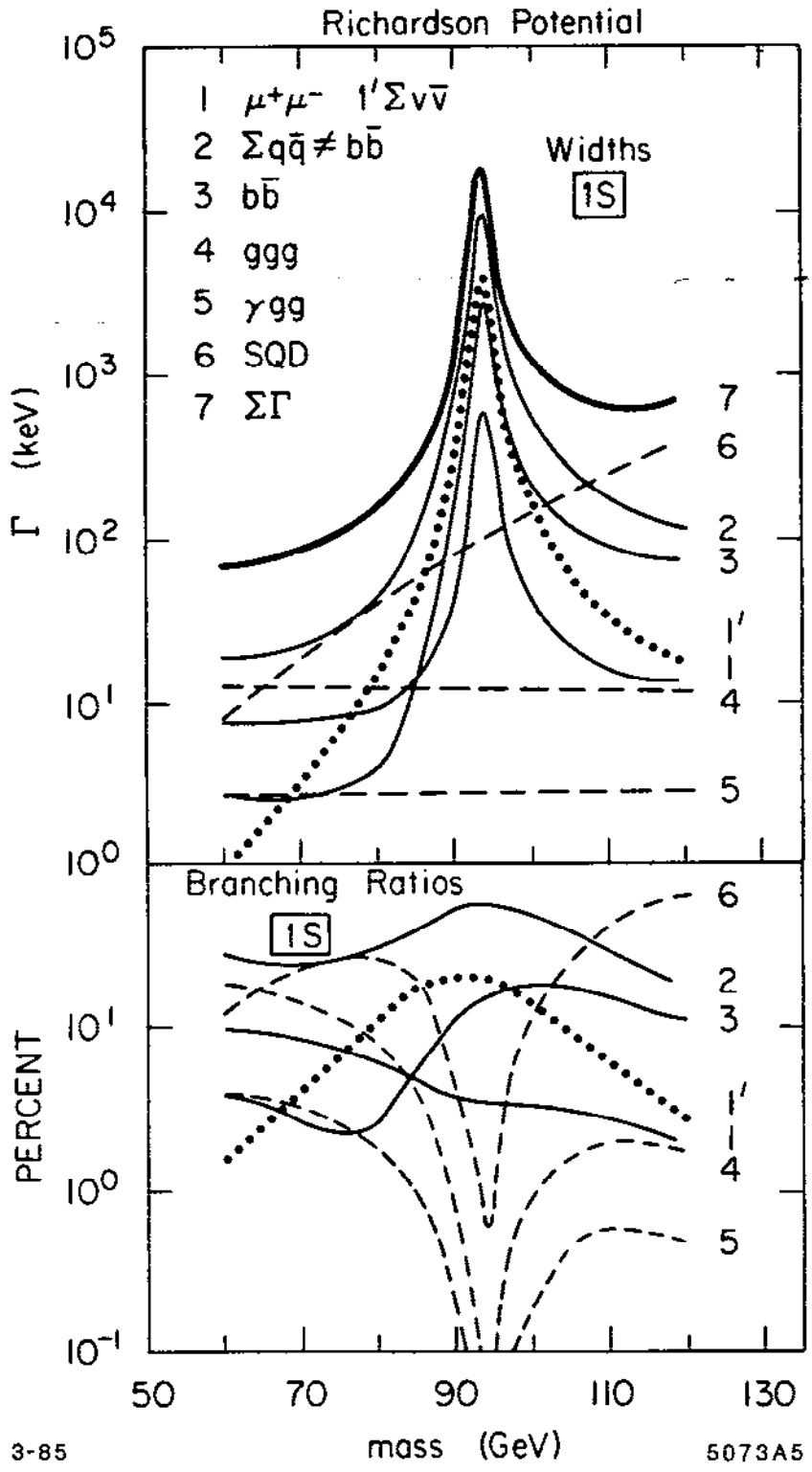
Richardson Potential
1 μ+μ− 1′Σνν̄
2 Σqq̄ ≠ bb̄
3 bb̄
4 ggg
5 γgg
6 SQD
7 ΣΓ
Widths
1S
Γ (keV)
Branching Ratios
1S
PERCENT
mass (GeV)
3-85
5073A5

Fig. 5

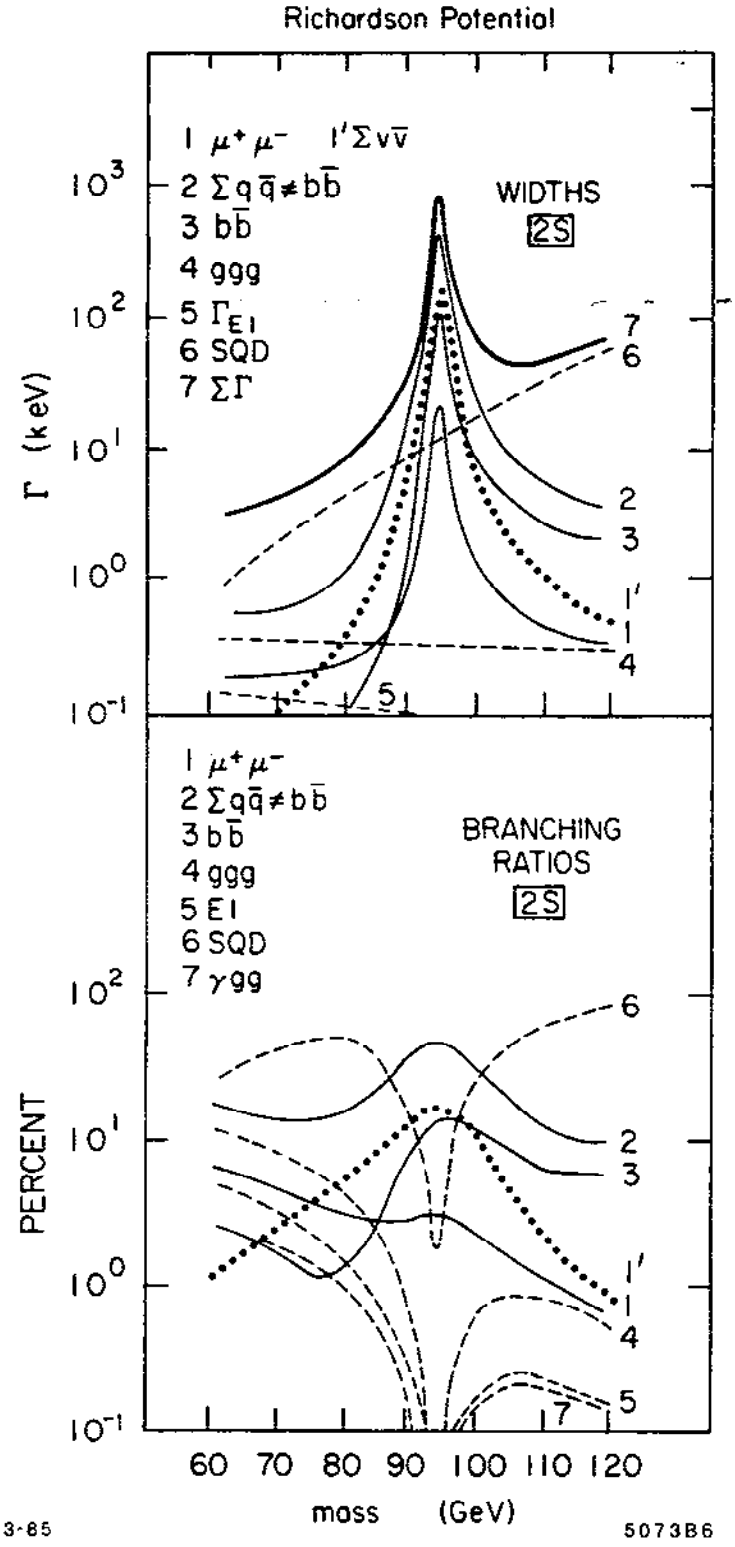
Richardson Potential
1 μ⁺μ⁻ 1'Σνν̄
2 Σqq̄≠bb̄
3 bb̄
4 ggg
5 Γ_E1
6 SQD
7 ΣΓ
WIDTHS
2S
Γ (keV)
10³
10²
10¹
10⁰
10⁻¹
1 μ⁺μ⁻
2 Σqq̄≠bb̄
3 bb̄
4 ggg
5 E1
6 SQD
7 γgg
BRANCHING RATIOS
2S
PERCENT
10²
10¹
10⁰
10⁻¹
60 70 80 90 100 110 120
mass (GeV)
3-85
5073B6

Fig. 6

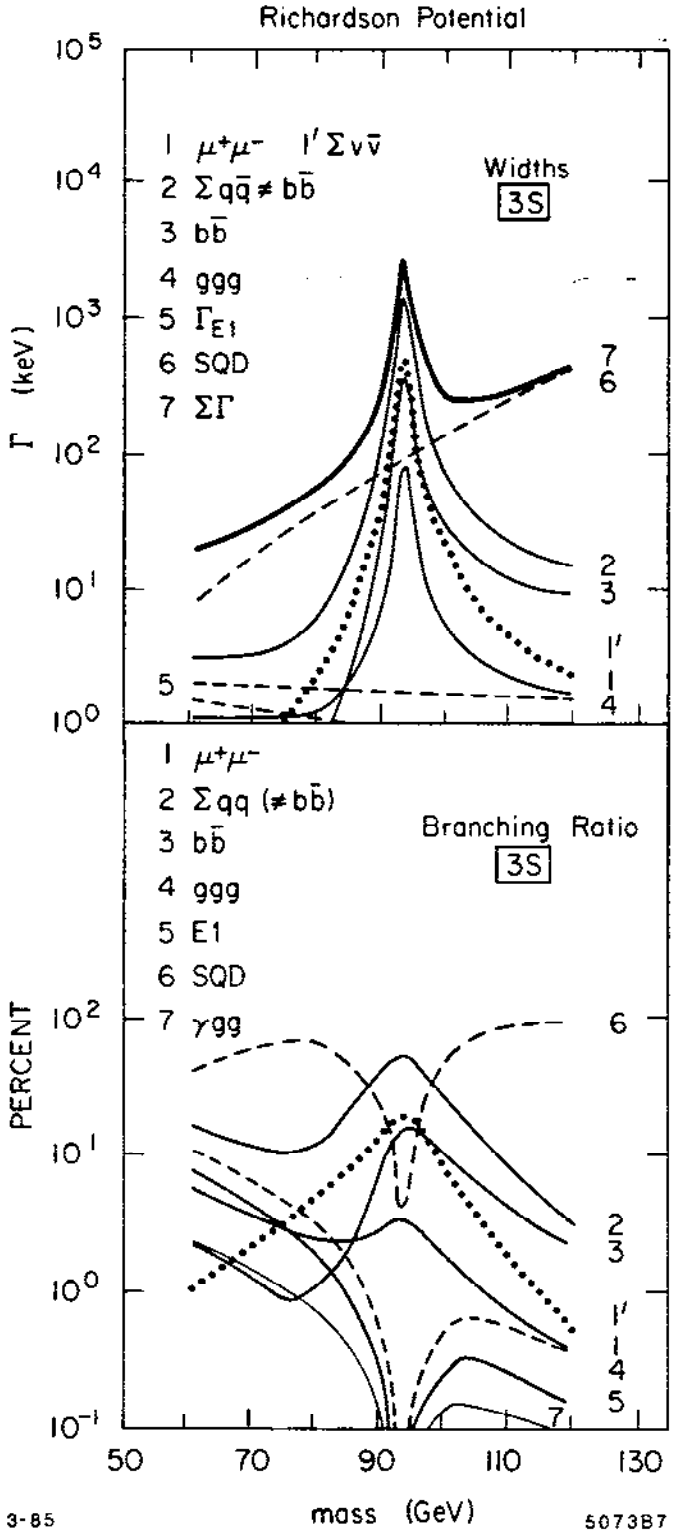
Richardson Potential
1 μ⁺μ⁻ l′ Σ ν ν̄
2 Σ qq̄ ≠ bb̄
3 bb̄
4 ggg
5 Γ_E1
6 SQD
7 ΣΓ
Widths
3S
Γ (keV)
10⁵
10⁴
10³
10²
10¹
10⁰
1 μ⁺μ⁻
2 Σ qq (≠ bb̄)
3 bb̄
4 ggg
5 E1
6 SQD
7 γgg
Branching Ratio
3S
PERCENT
10²
10¹
10⁰
10⁻¹
50
70
90
110
130
mass (GeV)
3-85
5073B7

Fig. 7

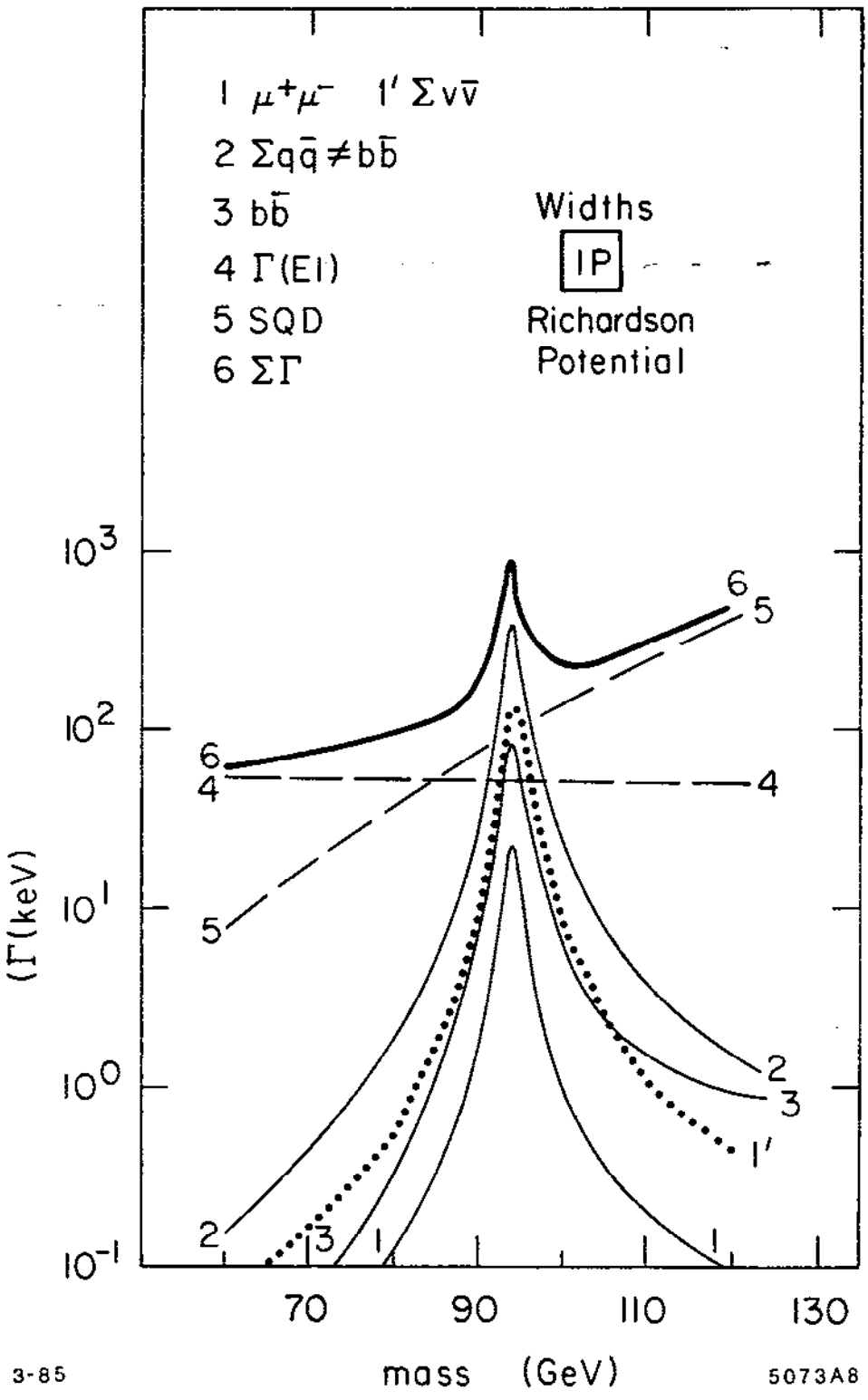
1 $\mu^+\mu^-$ 1' $\Sigma\nu\bar{\nu}$
2 $\Sigma q\bar{q} \neq b\bar{b}$
3 $b\bar{b}$
4 Γ(El)
5 SQD
6 $\Sigma\Gamma$
Widths
IP
Richardson
Potential
10^3
10^2
10^1
10^0
10^{-1}
(Γ(keV)
70
90
110
130
mass (GeV)
3-85
5073A8

Fig. 8

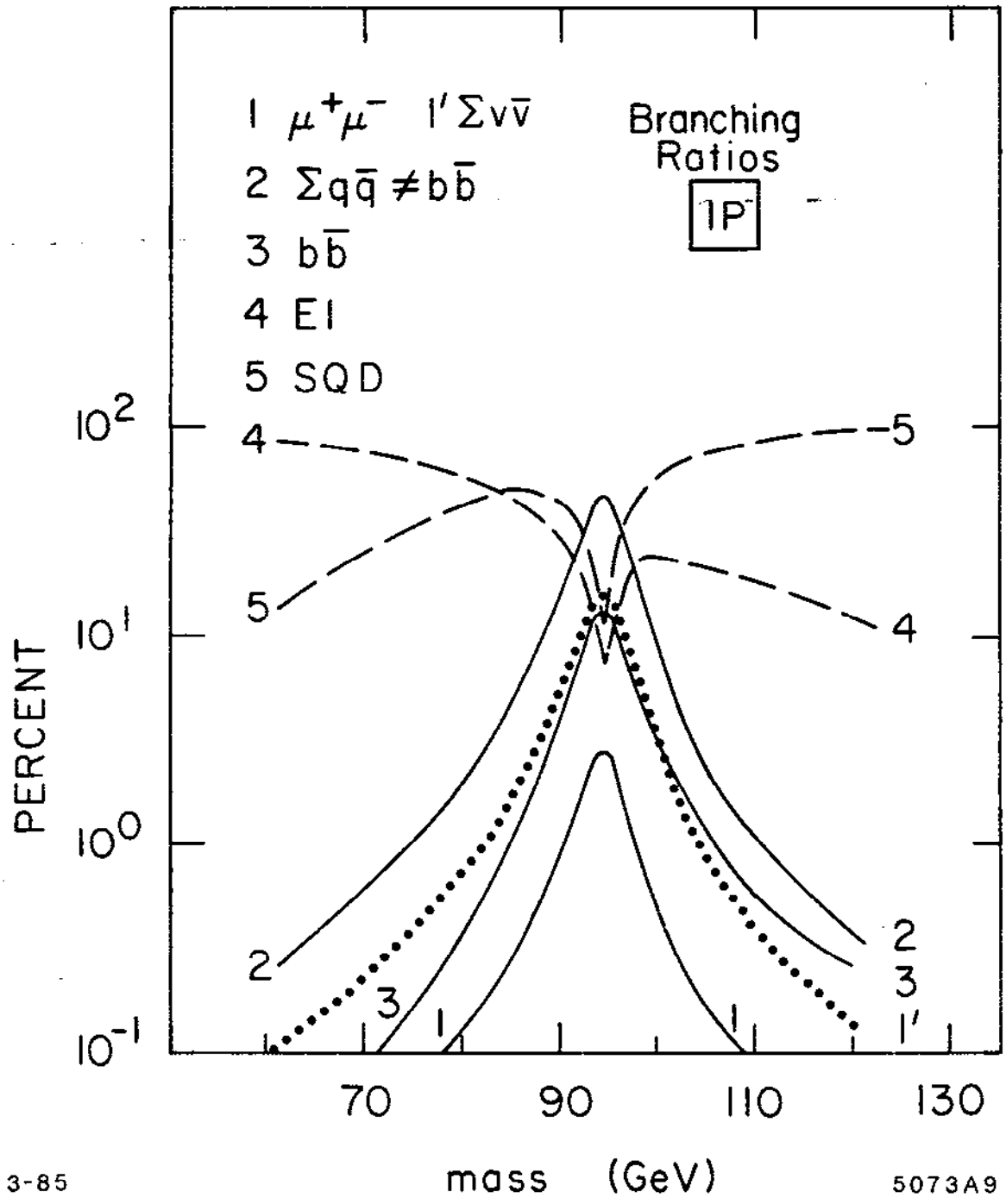
1 $\mu^+\mu^-$ l'Σνν̄
2 Σqq̄ ≠ bb̄
3 bb̄
4 EI
5 SQD
Branching Ratios
1P
PERCENT
10^2
10^1
10^0
10^{-1}
70
90
110
130
mass (GeV)
3-85
5073A9

Fig. 9

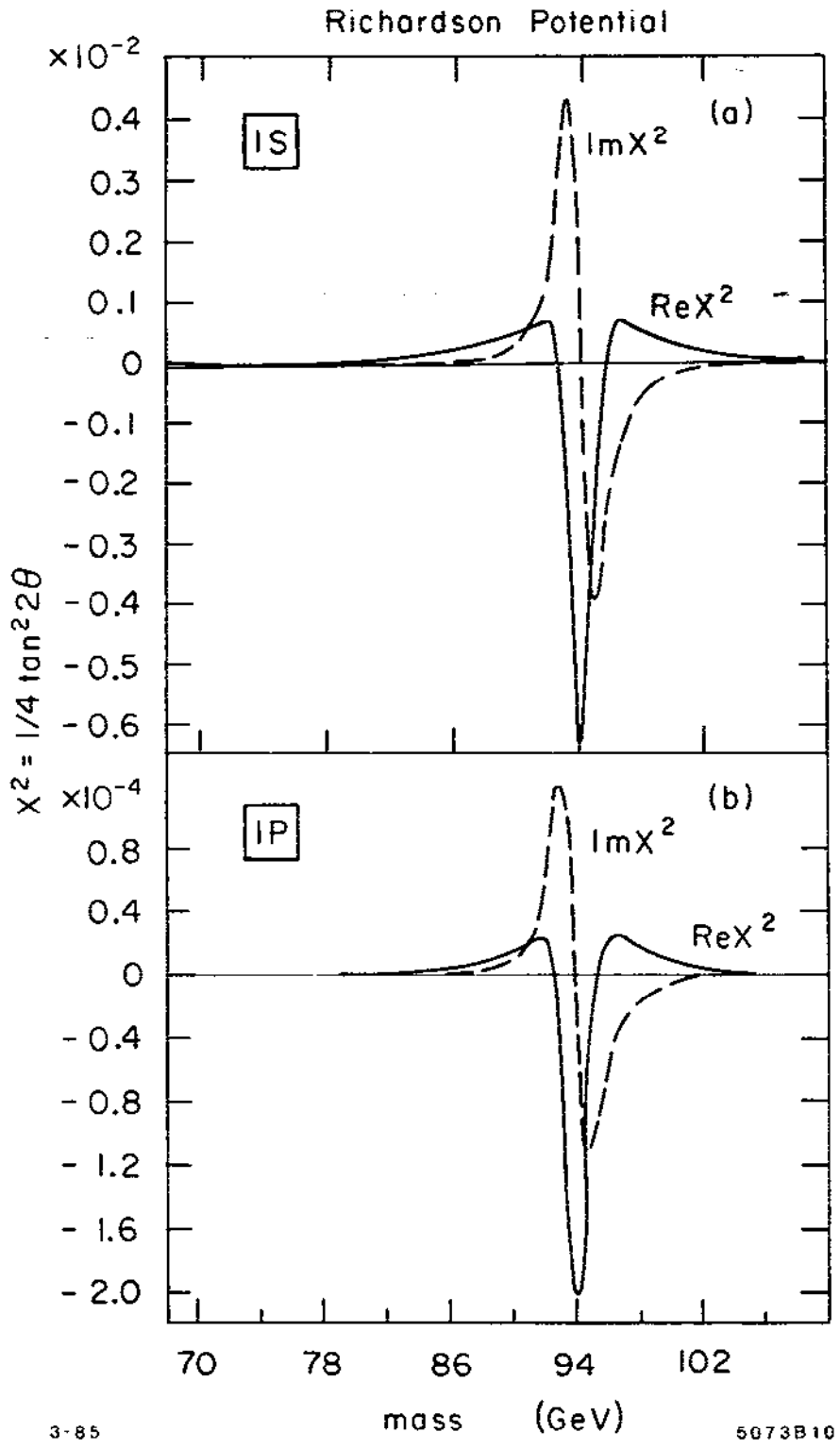
Richardson Potential
×10⁻²
0.4
0.3
0.2
0.1
0
-0.1
-0.2
-0.3
-0.4
-0.5
-0.6
IS
(a)
ImX²
ReX²
X² = 1/4 tan²2θ
×10⁻⁴
0.8
0.4
0
-0.4
-0.8
-1.2
-1.6
-2.0
IP
(b)
ImX²
ReX²
70
78
86
94
102
mass (GeV)
3-85
5073B10

Fig. 10

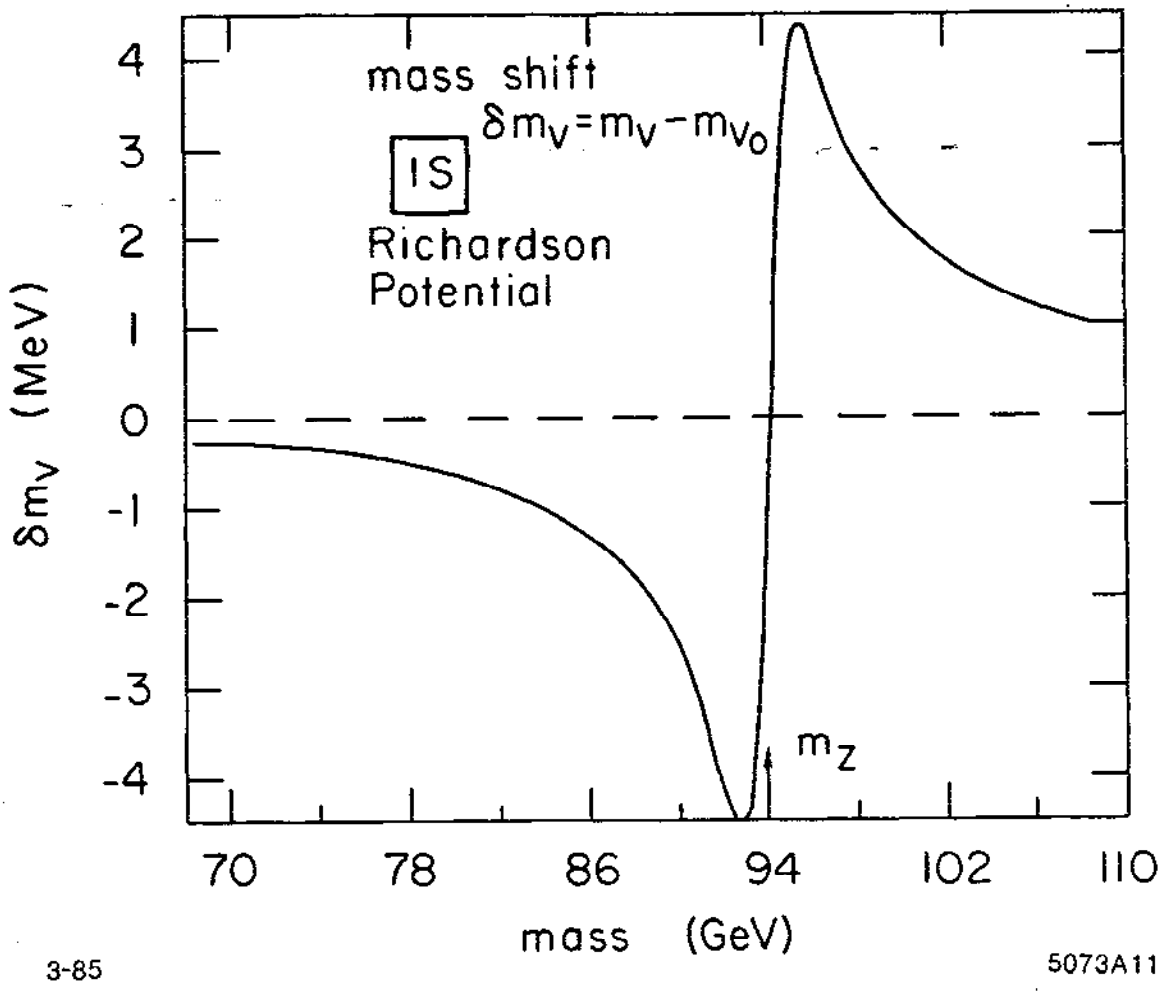
mass shift
$\delta m_V = m_V - m_{V_0}$
1S
Richardson
Potential
m_Z
δm_V (MeV)
4
3
2
1
0
-1
-2
-3
-4
70
78
86
94
102
110
mass (GeV)
3-85
5073A11

Fig. 11

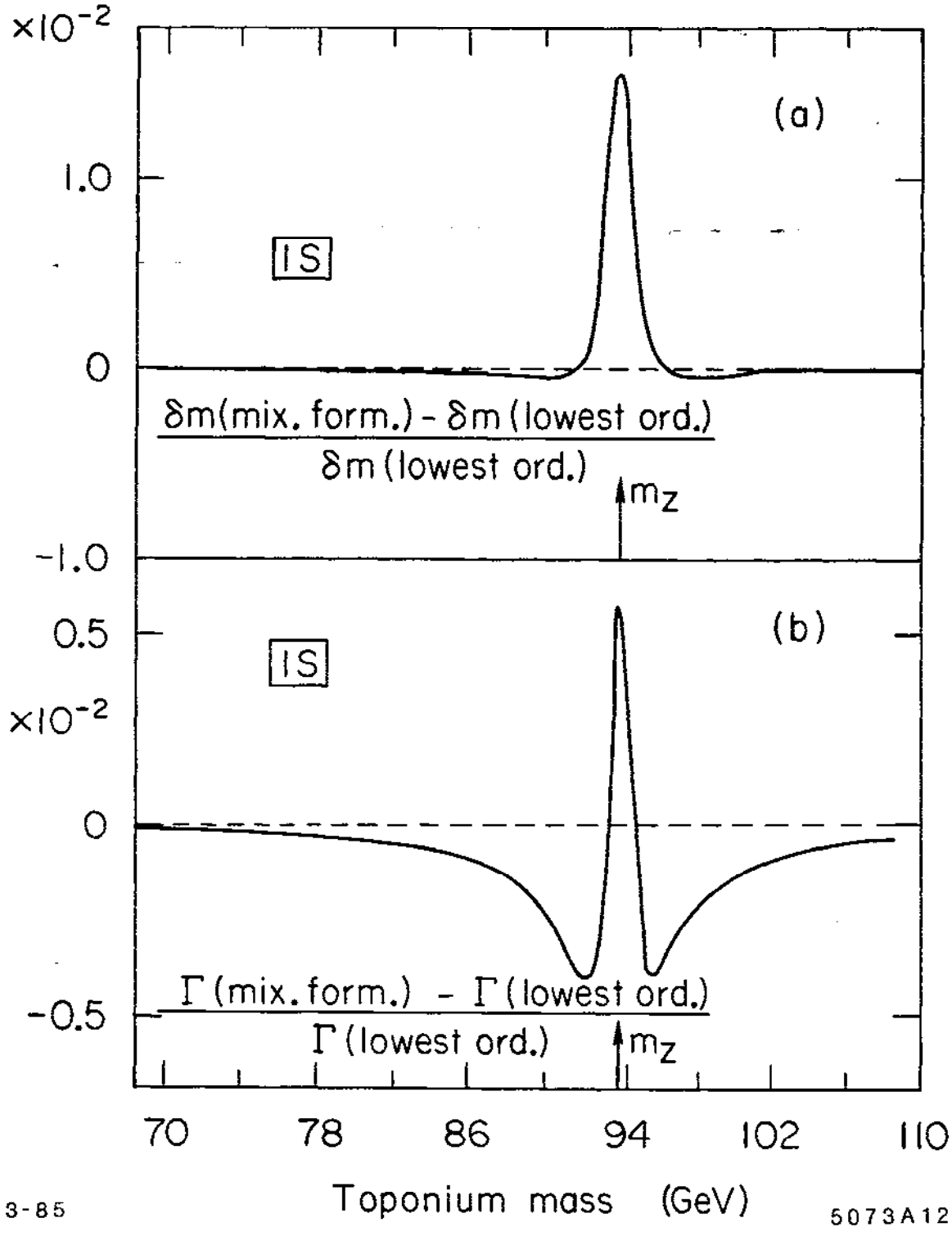
×10⁻²
1.0
0
-1.0
(a)
IS
δm(mix. form.) - δm (lowest ord.)
δm (lowest ord.)
mz
0.5
×10⁻²
0
-0.5
(b)
IS
Γ (mix. form.) - Γ (lowest ord.)
Γ (lowest ord.)
mz
70
78
86
94
102
110
Toponium mass (GeV)
3-85
5073A12

Fig. 12

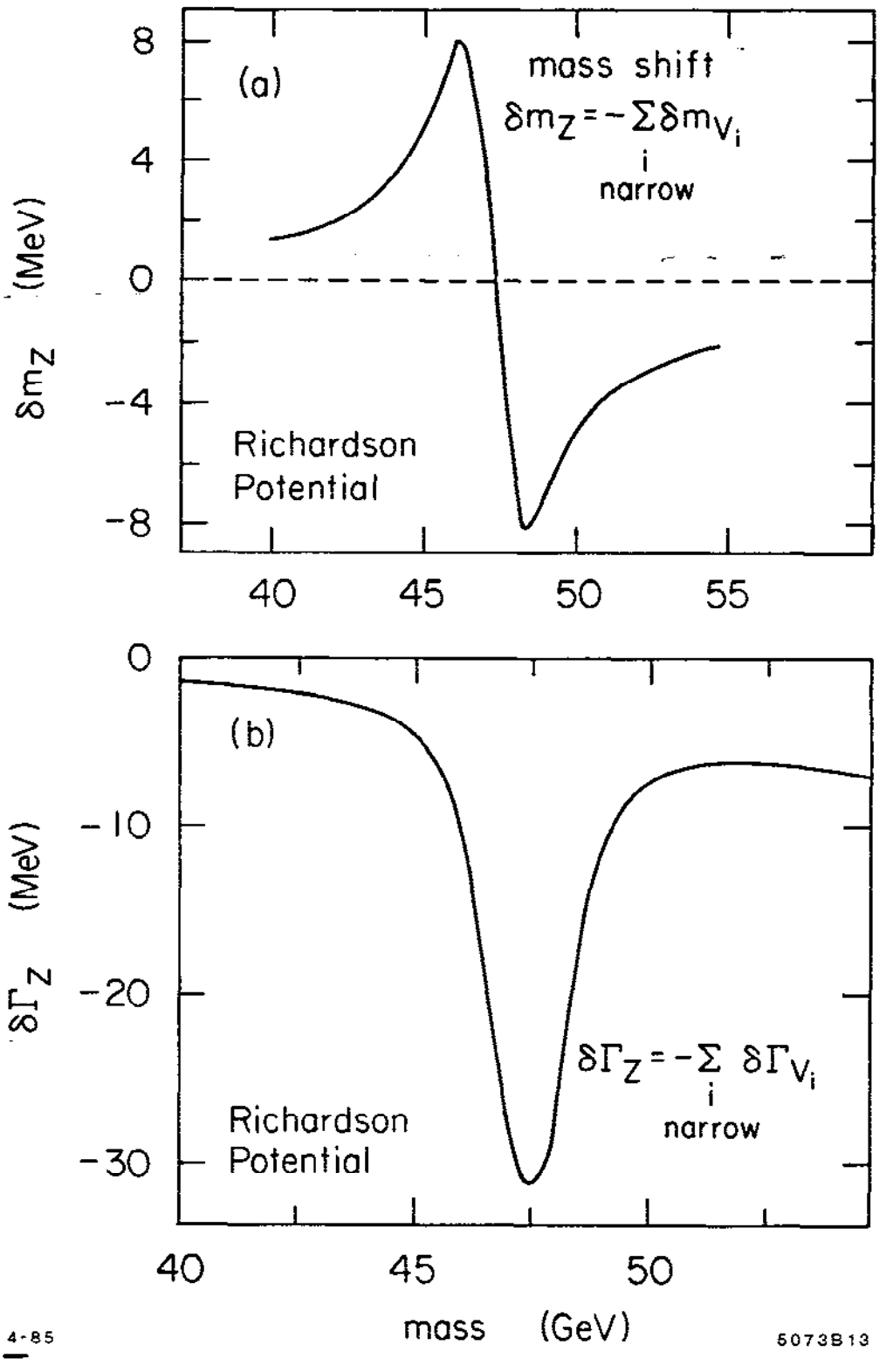
(a)
mass shift
$\delta m_Z = -\sum_i \delta m_{V_i}$
narrow
Richardson
Potential
δm_Z (MeV)
8
4
0
-4
-8
40
45
50
55
(b)
$\delta\Gamma_Z = -\sum_i \delta\Gamma_{V_i}$
narrow
Richardson
Potential
$\delta\Gamma_Z$ (MeV)
0
-10
-20
-30
40
45
50
mass (GeV)
4-85
5073B13

Fig. 13

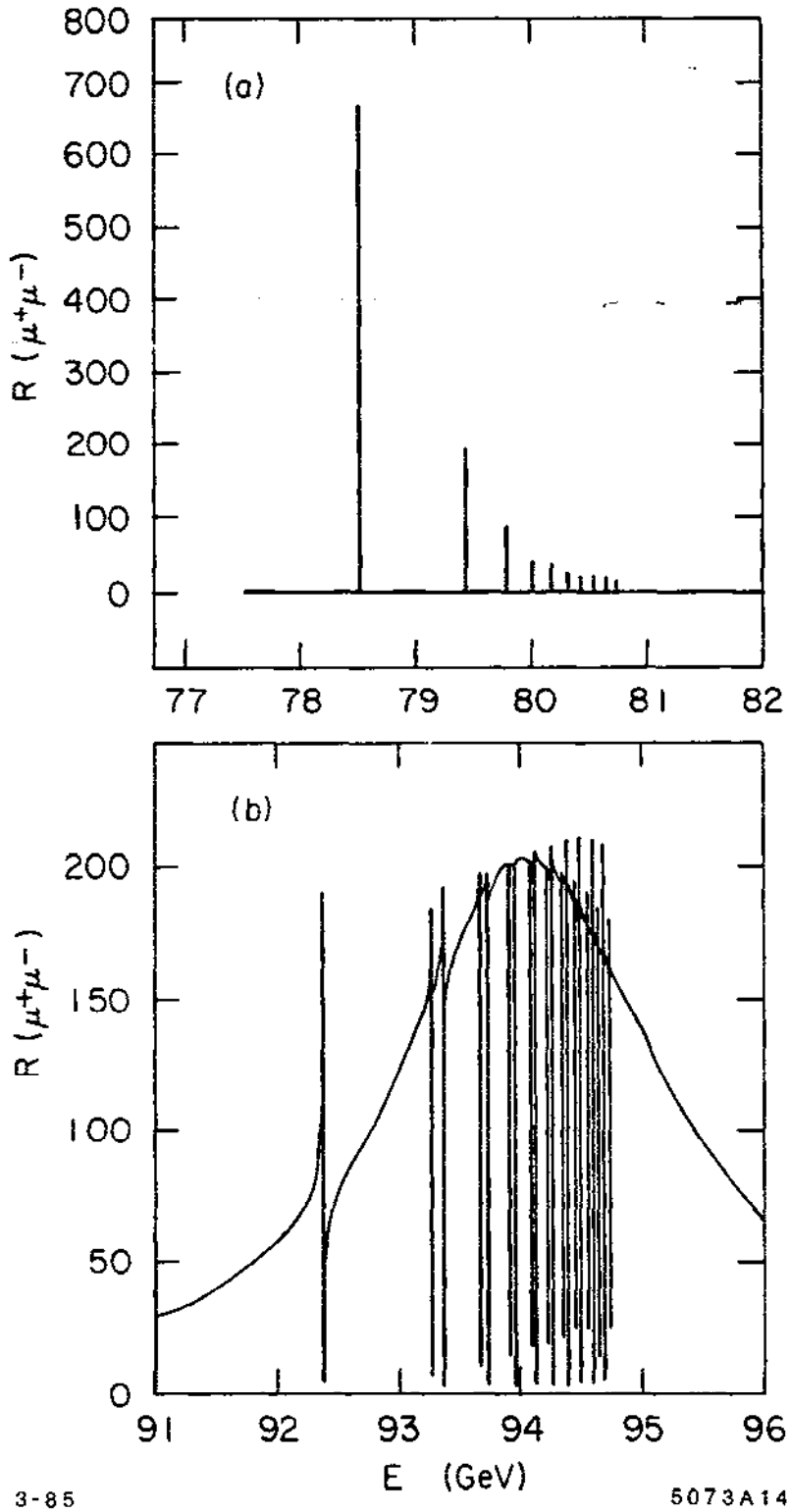
(a)
800
700
600
500
400
300
200
100
0
R ($\mu^+\mu^-$)
77
78
79
80
81
82
(b)
200
150
100
50
0
R ($\mu^+\mu^-$)
91
92
93
94
95
96
E (GeV)
3-85
5073A14

Fig. 14

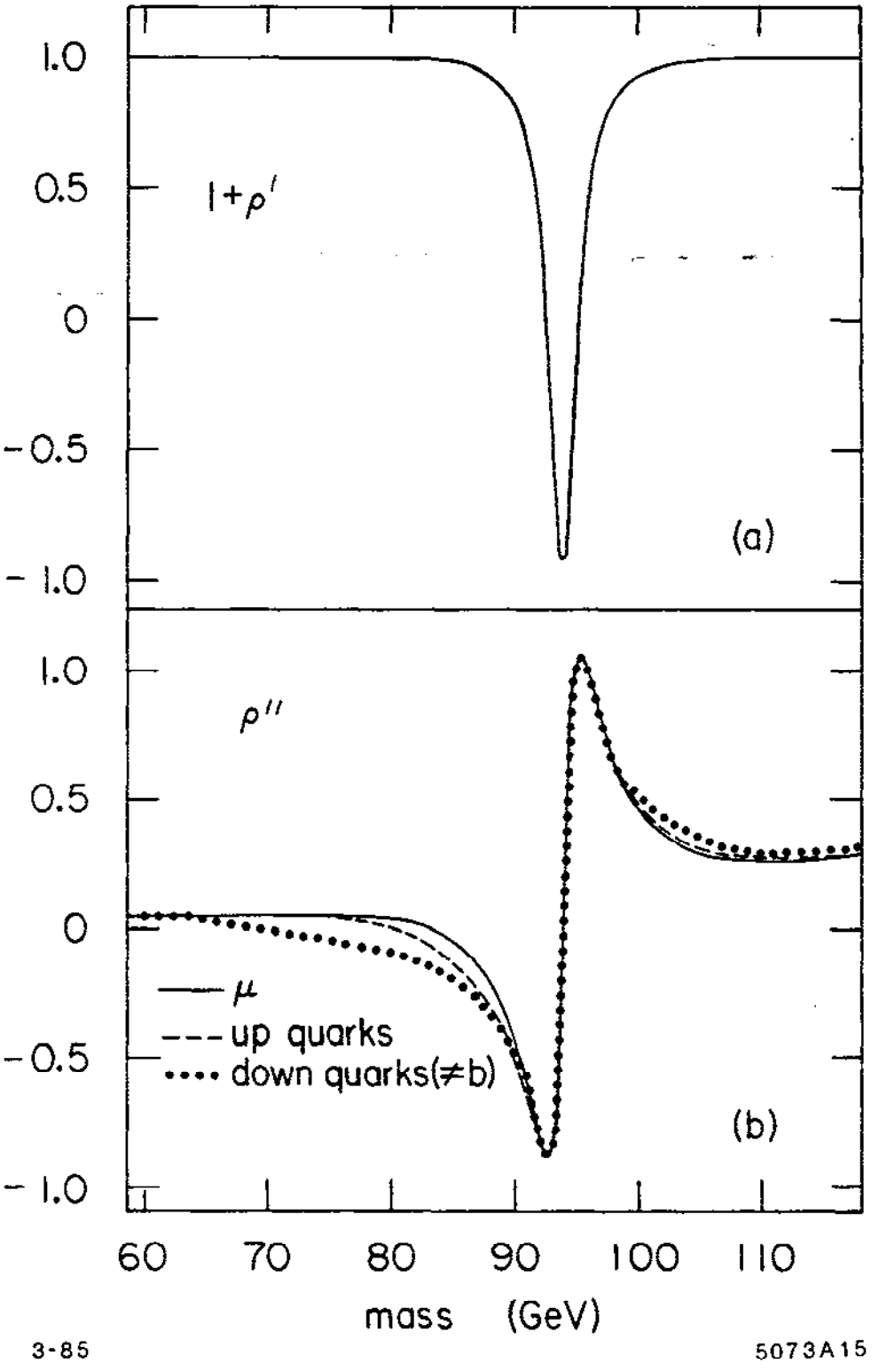
1.0
0.5
0
-0.5
-1.0
1+ρ'
(a)
1.0
0.5
0
-0.5
-1.0
ρ''
μ
up quarks
down quarks(≠b)
(b)
60
70
80
90
100
110
mass (GeV)
3-85
5073A15

Fig. 15

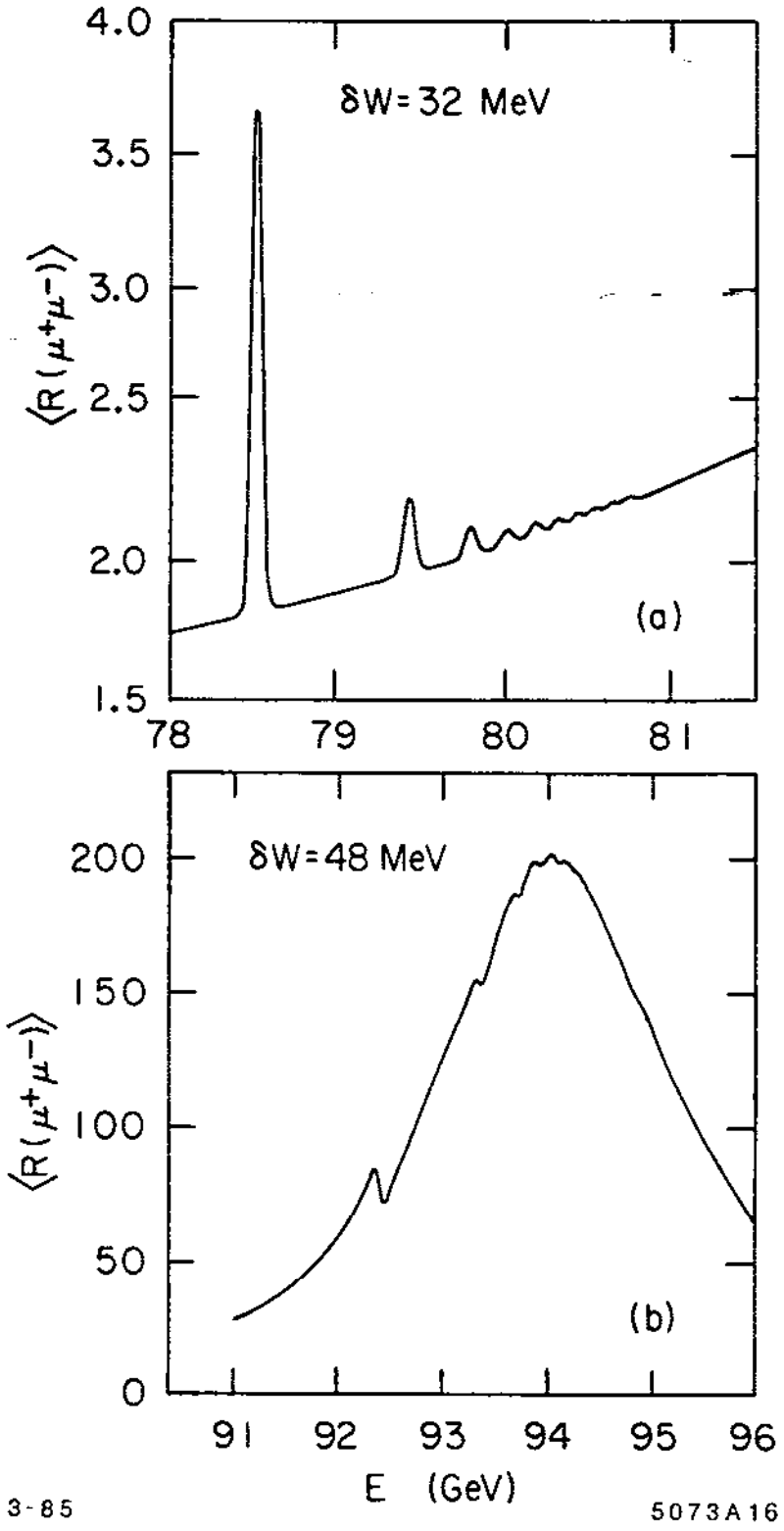
4.0
3.5
3.0
2.5
2.0
1.5
δW=32 MeV
⟨R(μ+μ−)⟩
(a)
78
79
80
81
200
150
100
50
0
δW=48 MeV
⟨R(μ+μ−)⟩
(b)
91
92
93
94
95
96
E (GeV)
3-85
5073A16

Fig. 16

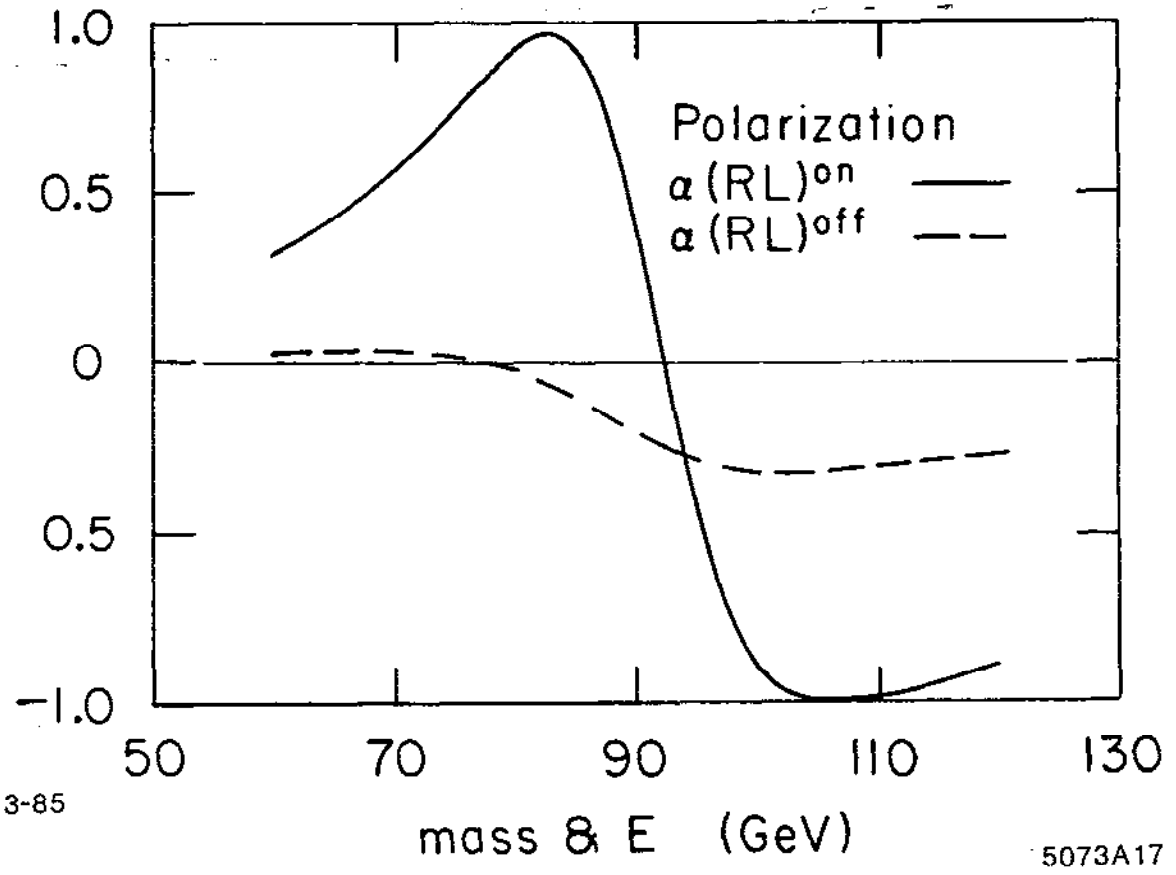
1.0
0.5
0
0.5
-1.0
50
70
90
110
130
Polarization
α(RL)on
α(RL)off
3-85
mass & E (GeV)
5073A17

Fig. 17

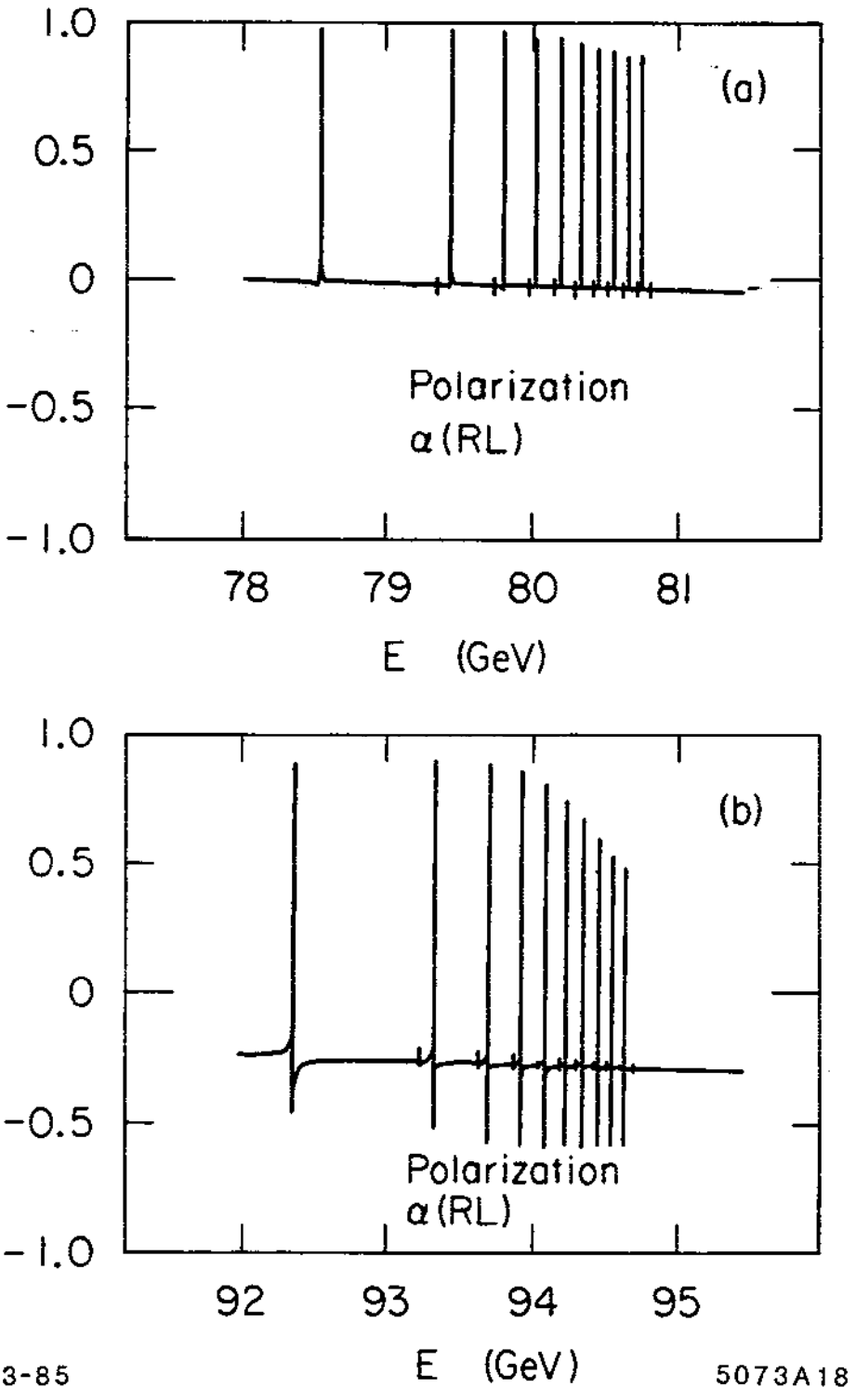
1.0
0.5
0
-0.5
-1.0
(a)
Polarization
α(RL)
78
79
80
81
E (GeV)
1.0
0.5
0
-0.5
-1.0
(b)
Polarization
α(RL)
92
93
94
95
E (GeV)
3-85
5073A18

Fig. 18

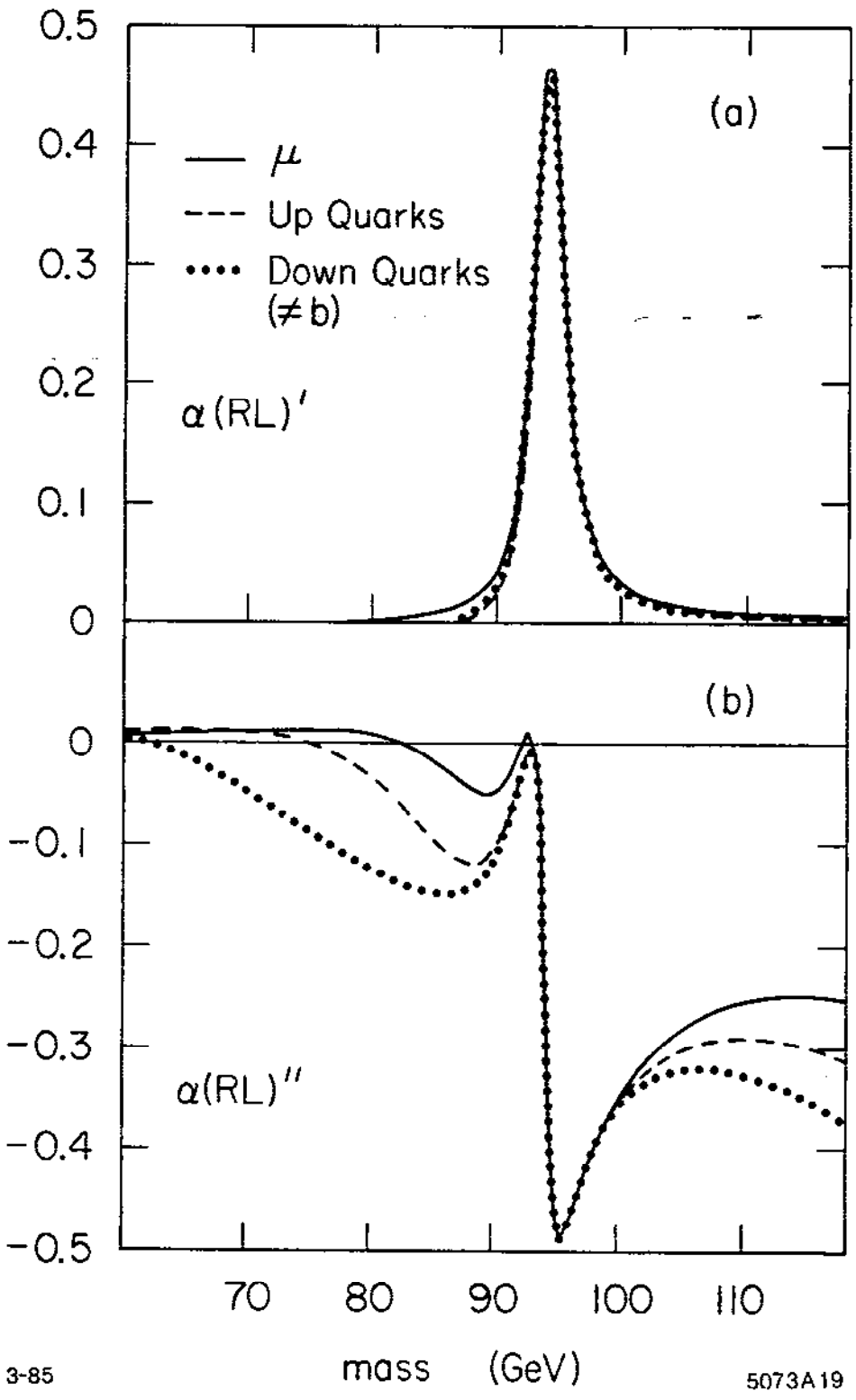
0.5
0.4
0.3
0.2
0.1
0
(a)
μ
Up Quarks
Down Quarks
(≠b)
α(RL)′
(b)
0
−0.1
−0.2
−0.3
−0.4
−0.5
α(RL)″
70
80
90
100
110
mass (GeV)
3-85
5073A19

Fig. 19

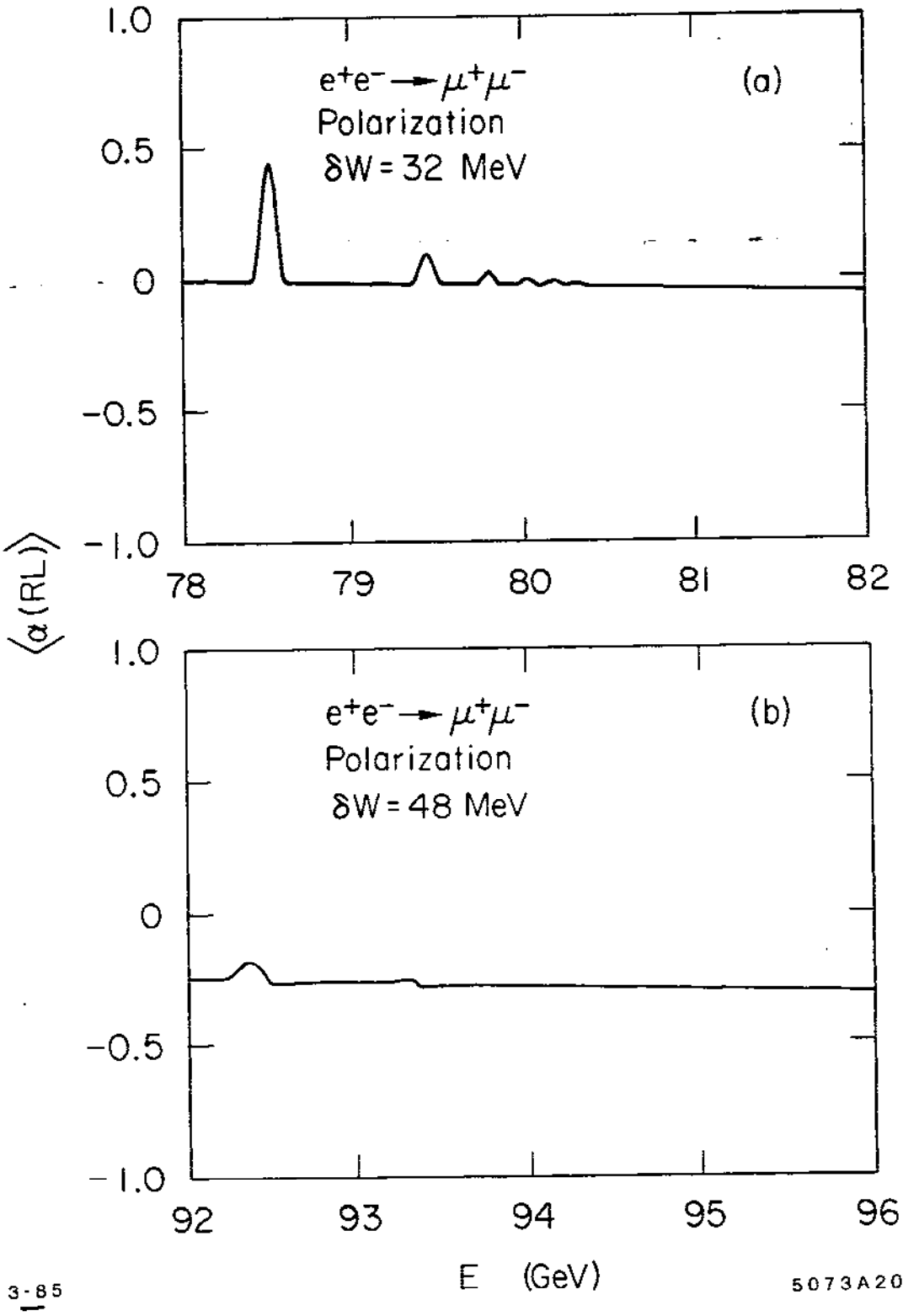
1.0
0.5
0
-0.5
-1.0
$e^+e^- \rightarrow \mu^+\mu^-$
(a)
Polarization
δW = 32 MeV
78
79
80
81
82
$\langle a(RL) \rangle$
1.0
0.5
0
-0.5
-1.0
$e^+e^- \rightarrow \mu^+\mu^-$
(b)
Polarization
δW = 48 MeV
92
93
94
95
96
E (GeV)
3-85
5073A20

Fig. 20

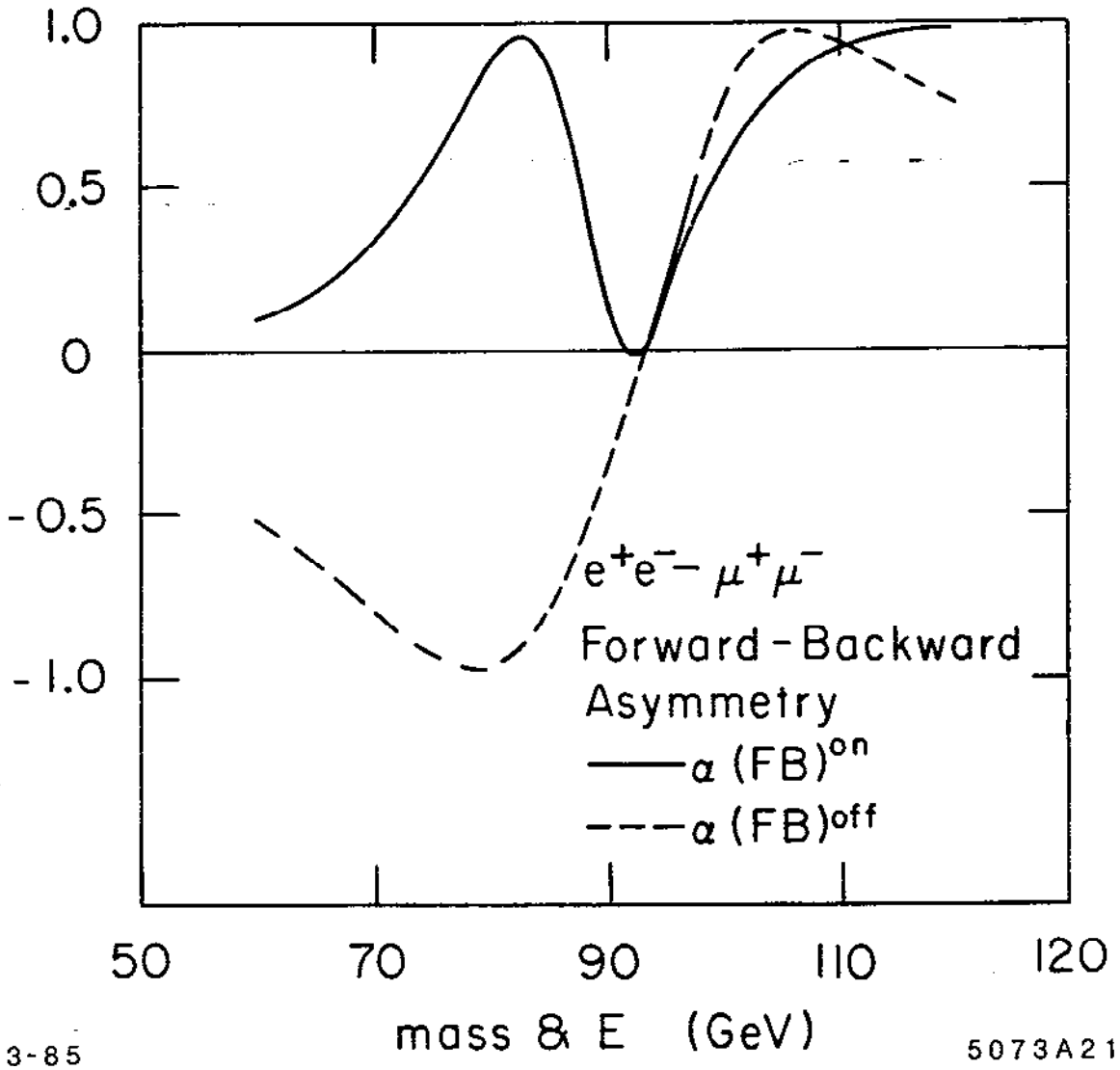
1.0
0.5
0
-0.5
-1.0
50
70
90
110
120
mass & E (GeV)
$e^+e^- \mu^+\mu^-$
Forward - Backward
Asymmetry
α (FB)^{on}
α (FB)^{off}
3-85
5073A21

Fig. 21

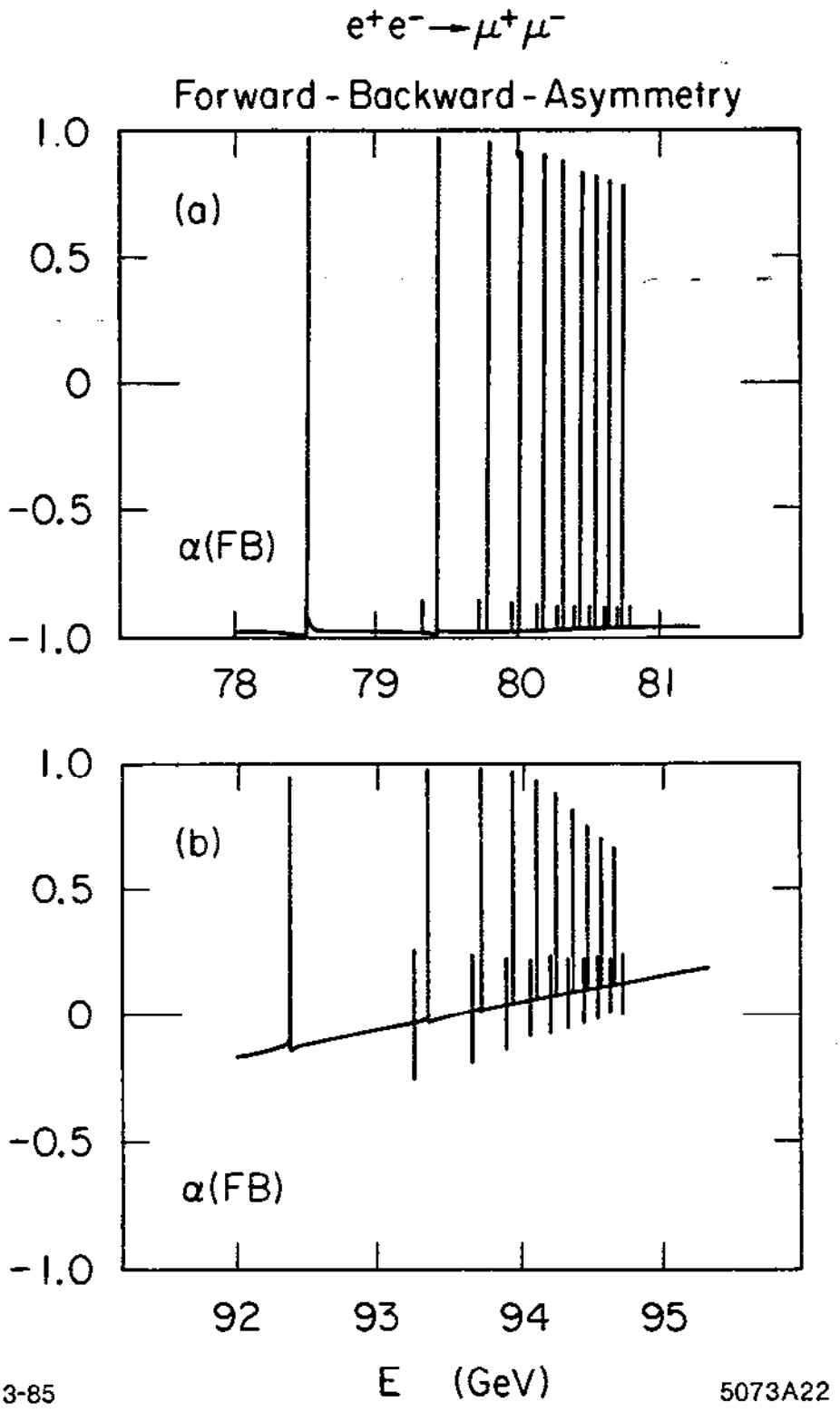
$e^+e^- \to \mu^+\mu^-$
Forward - Backward - Asymmetry
1.0
0.5
0
-0.5
-1.0
(a)
α(FB)
78
79
80
81
1.0
0.5
0
-0.5
-1.0
(b)
α(FB)
92
93
94
95
E (GeV)
3-85
5073A22

Fig. 22

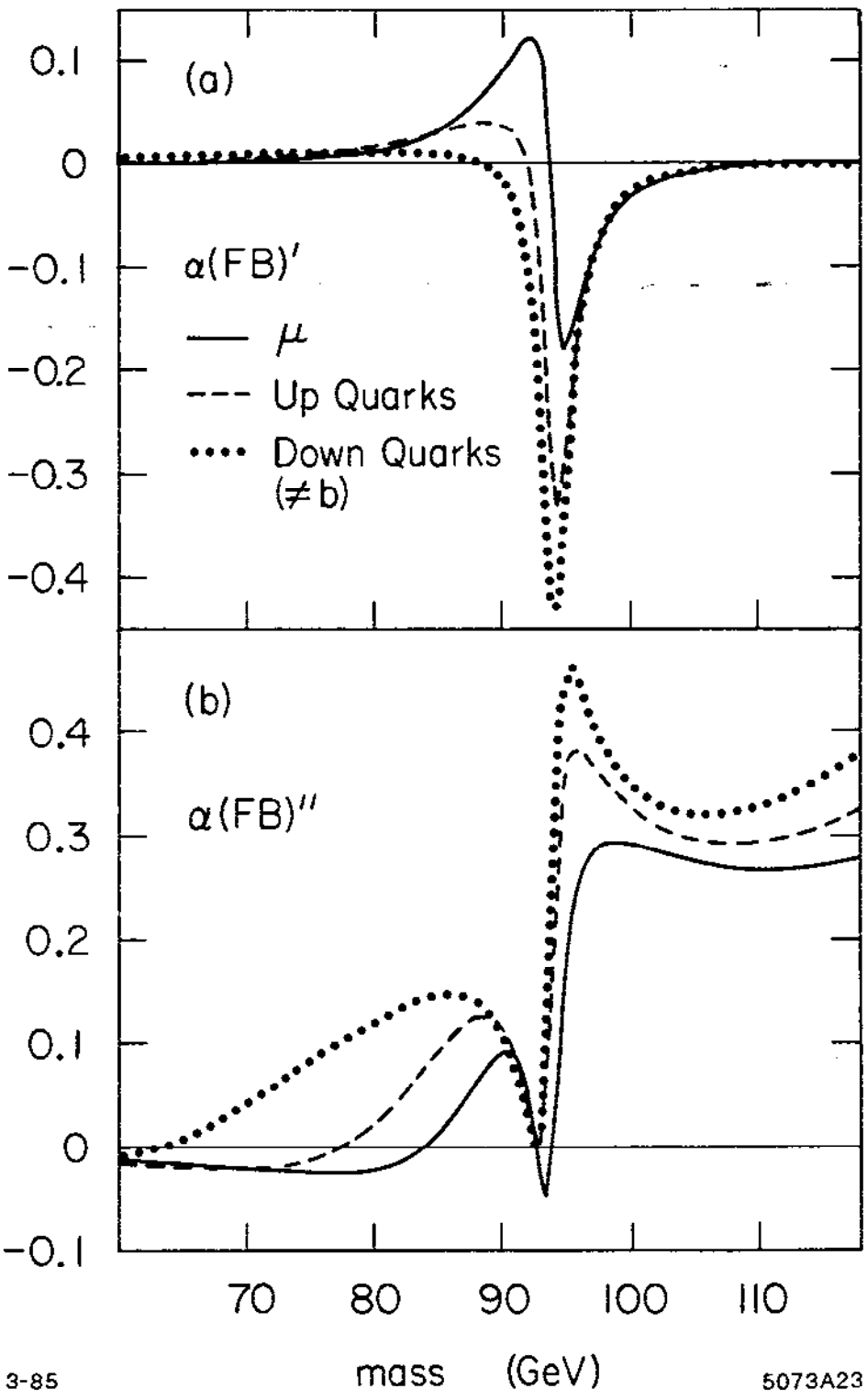
(a)
α(FB)′
μ
Up Quarks
Down Quarks
(≠b)
(b)
α(FB)″
0.1
0
-0.1
-0.2
-0.3
-0.4
0.4
0.3
0.2
0.1
0
-0.1
70
80
90
100
110
mass (GeV)
3-85
5073A23

Fig. 23

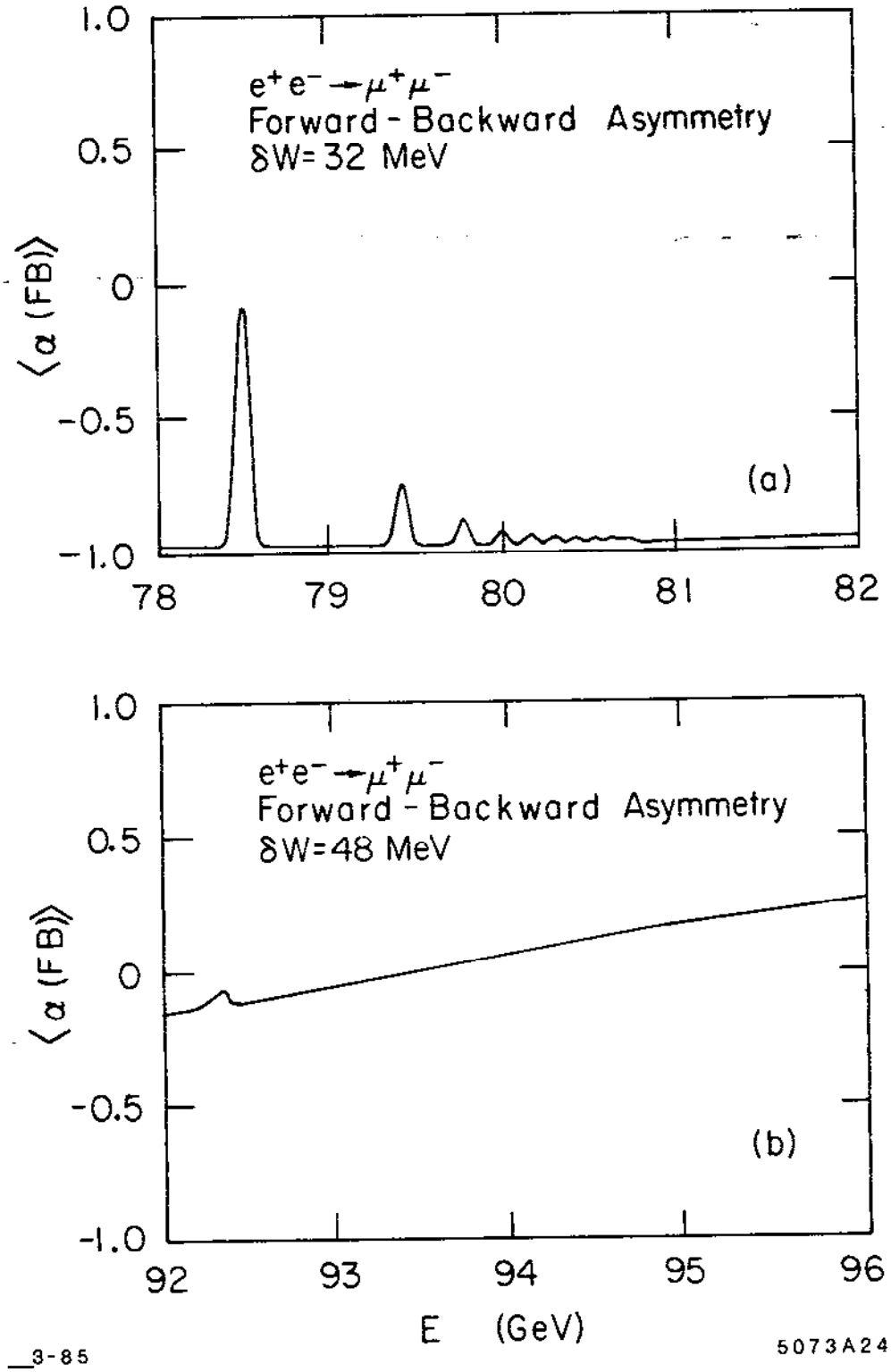
1.0
0.5
0
-0.5
-1.0
⟨α (FB)⟩
e+e− → μ+μ−
Forward - Backward Asymmetry
δW= 32 MeV
(a)
78
79
80
81
82
1.0
0.5
0
-0.5
-1.0
⟨α (FB)⟩
e+e− → μ+μ−
Forward - Backward Asymmetry
δW=48 MeV
(b)
92
93
94
95
96
E (GeV)
3-85
5073A24

Fig. 24

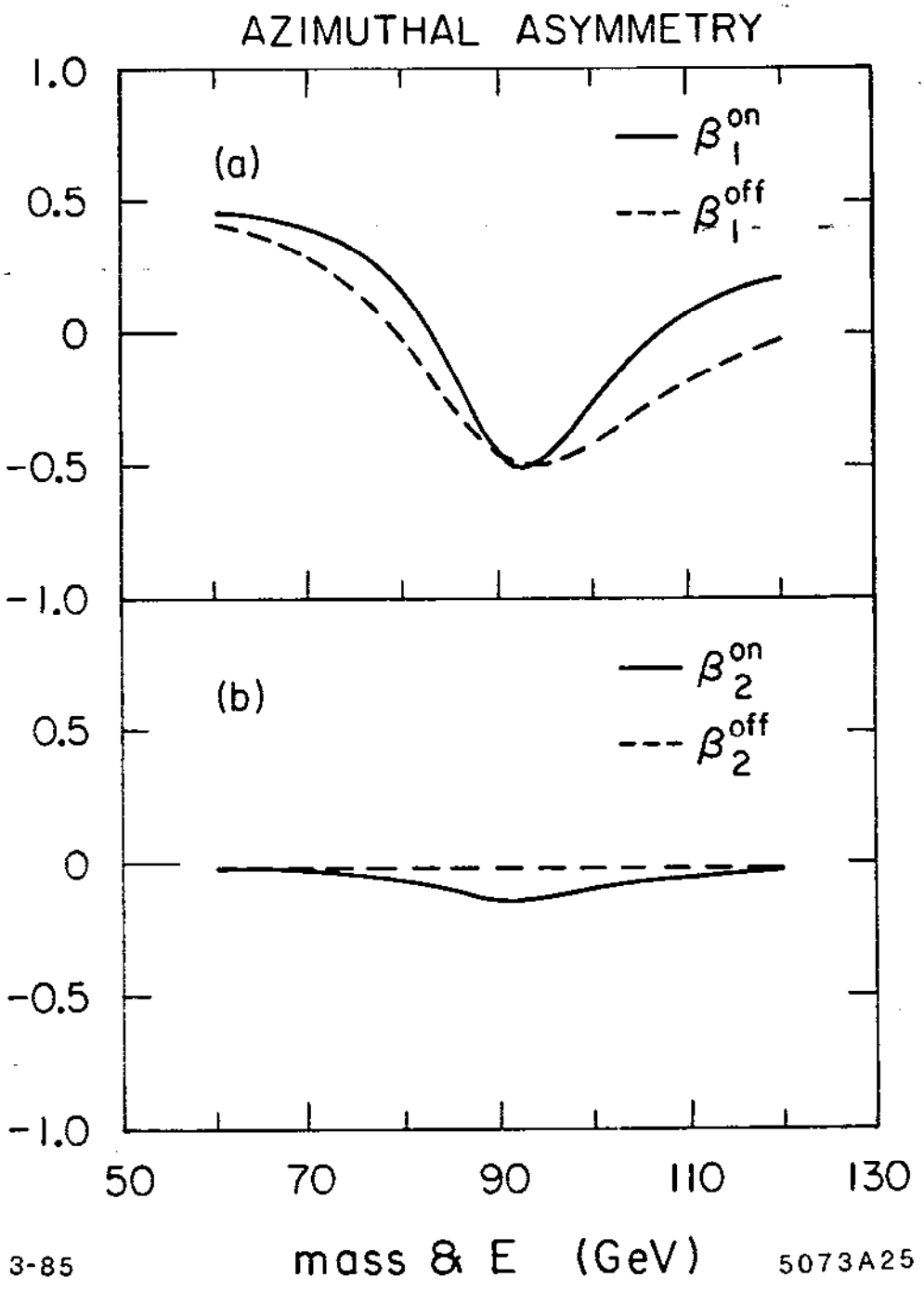
AZIMUTHAL ASYMMETRY
1.0
0.5
0
-0.5
-1.0
(a)
β_1^{on}
β_1^{off}
(b)
β_2^{on}
β_2^{off}
50
70
90
110
130
mass & E (GeV)
3-85
5073A25

Fig. 25

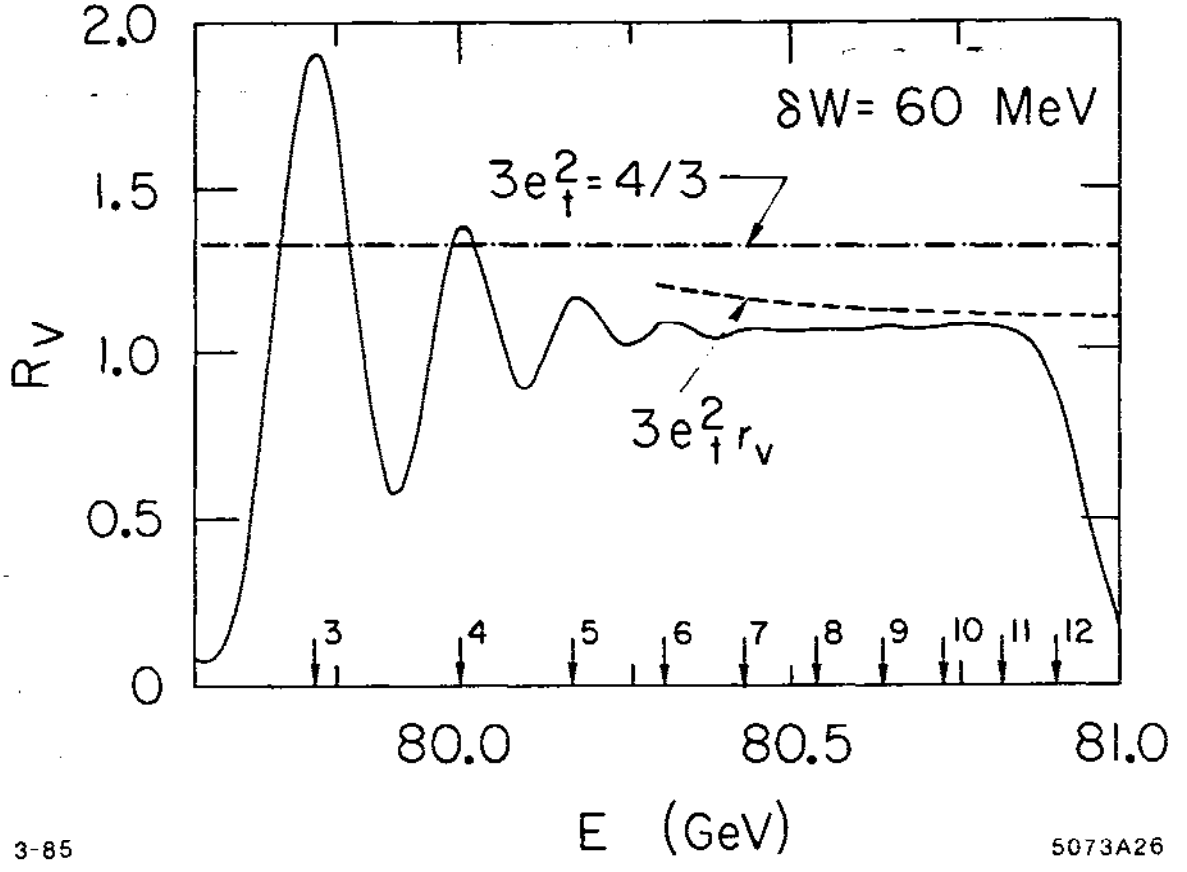
2.0
1.5
1.0
0.5
0
R_V
$\delta W = 60$ MeV
$3e_f^2 = 4/3$
$3e_f^2 r_v$
3
4
5
6
7
8
9
10
11
12
80.0
80.5
81.0
E (GeV)
3-85
5073A26

Fig. 26

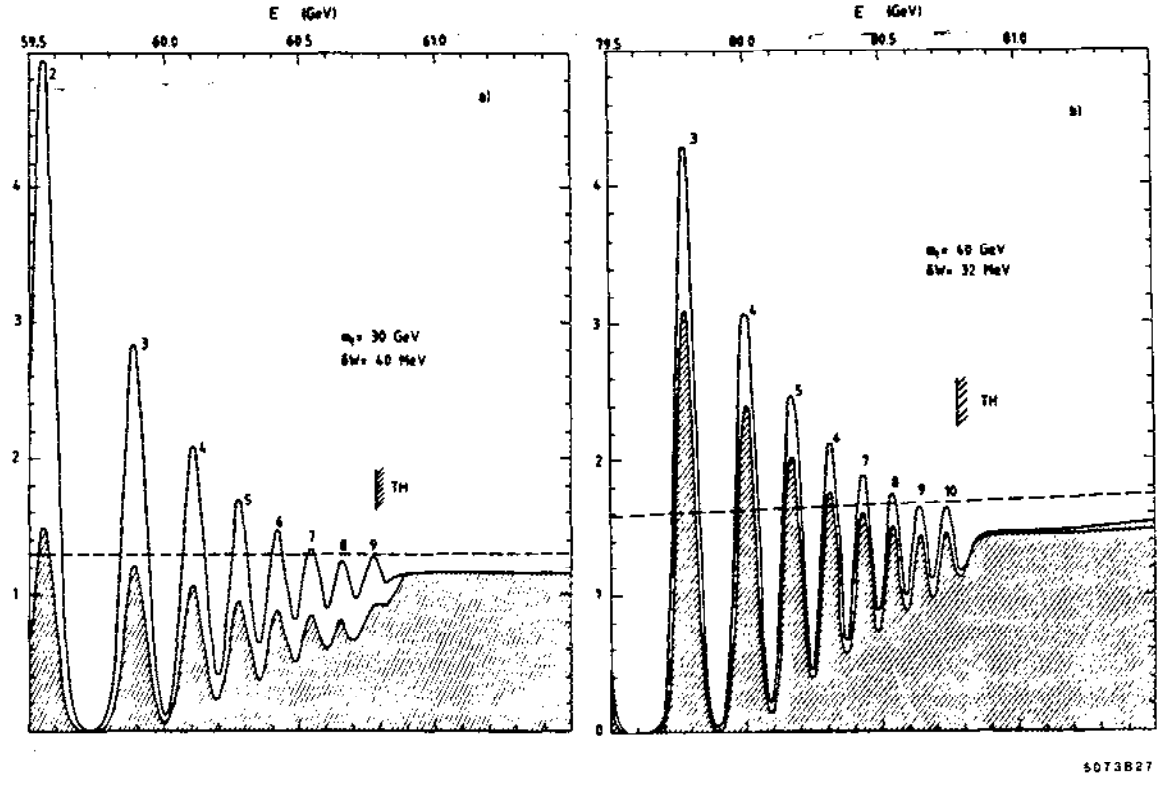
E (GeV)
59.5
60.0
60.5
61.0
a)
m_H= 30 GeV
δW= 40 MeV
TH
E (GeV)
79.5
80.0
80.5
81.0
b)
m_H= 60 GeV
δW= 32 MeV
TH
5073B27

Fig. 27

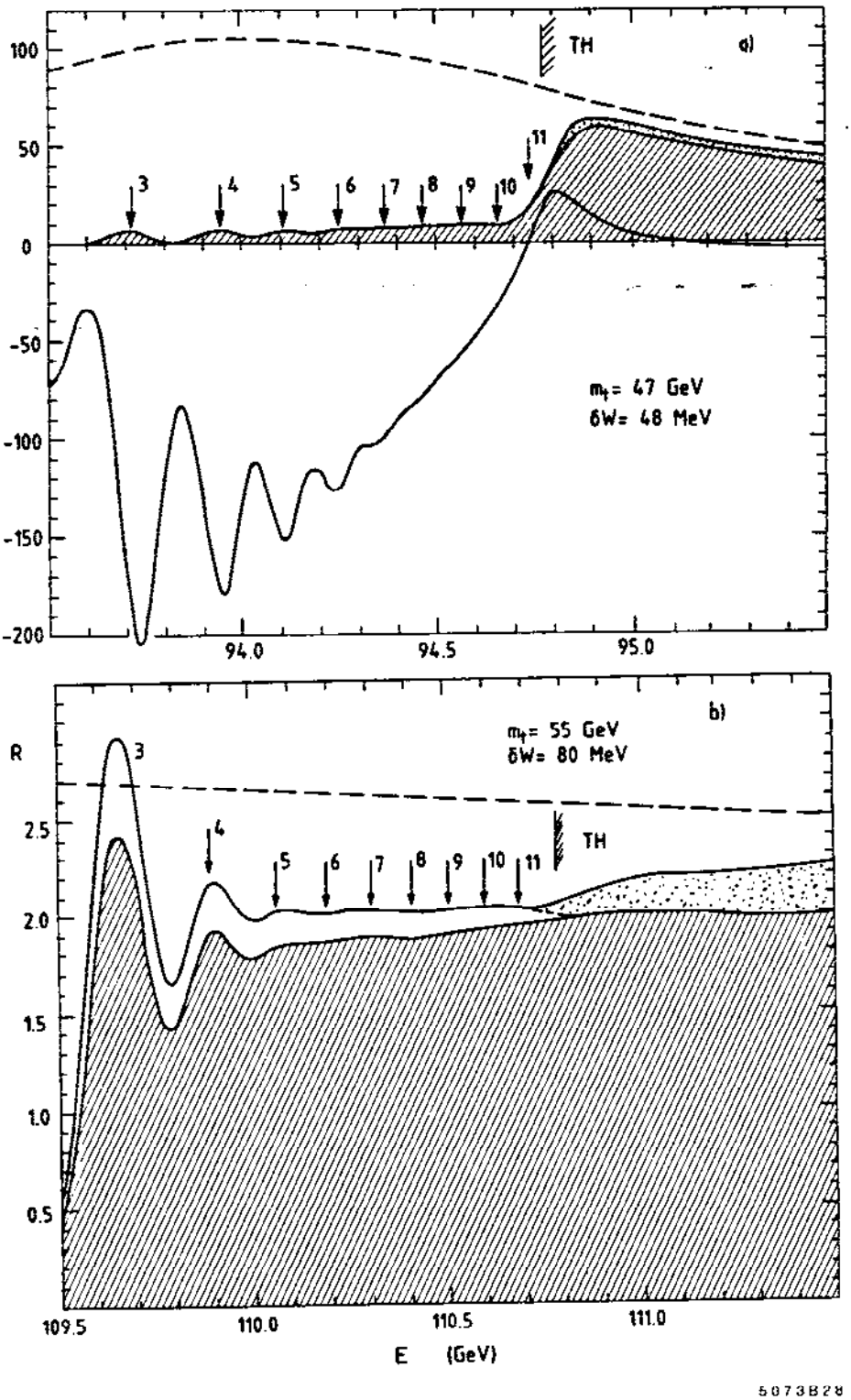
a)
TH
3
4
5
6
7
8
9
10
11
100
50
0
-50
-100
-150
-200
94.0
94.5
95.0
m_t= 47 GeV
δW= 48 MeV
b)
m_t= 55 GeV
δW= 80 MeV
R
2.5
2.0
1.5
1.0
0.5
109.5
110.0
110.5
111.0
E (GeV)
5073B28

Fig. 28